How Proteins Trigger Excitation Energy Transfer in the FMO Complex of Green Sulfur Bacteria

J. Adolphs and T. Renger

Institut für Chemie und Biochemie, Freie Universität Berlin, Berlin, Germany

ABSTRACT   A simple electrostatic method for the calculation of optical transition energies of pigments in protein environments is presented and applied to the Fenna-Matthews-Olson (FMO) complex of Prosthecochloris aestuarii and Chlorobium tepidum. The method, for the first time, allows us to reach agreement between experimental optical spectra and calculations based on transition energies of pigments that are calculated in large part independently, rather than fitted to the spectra. In this way it becomes possible to understand the molecular mechanism allowing the protein to trigger excitation energy transfer reactions. The relative shift in excitation energies of the seven bacteriochlorophyll-a pigments of the FMO complex of P. aestuarii and C. tepidum are obtained from calculations of electrochromic shifts due to charged amino acids, assuming a standard protonation pattern of the protein, and by taking into account the three different ligand types of the pigments. The calculations provide an explanation of some of the earlier results for the transition energies obtained from fits of optical spectra. In addition, those earlier fits are verified here by using a more advanced theory of optical spectra, a genetic algorithm, and excitonic couplings obtained from electrostatic calculations that take into account the influence of the dielectric protein environment. The two independent calculations of site energies strongly favor one of the two possible orientations of the FMO trimer relative to the photosynthetic membrane, which were identified by electron microscopic studies and linear dichroism experiments. Efficient transfer of excitation energy to the reaction center requires bacteriochlorophylls 3 and 4 to be the linker pigments. The temporal and spatial transfer of excitation energy through the FMO complex is calculated to proceed along two branches, with transfer times that differ by an order of magnitude.

INTRODUCTION

In photosynthetic antennae, light is absorbed by pigments and the excitation energy is transferred to the photosynthetic reaction center. The pigments are held by a protein scaffold at the right distances and orientations for efficient excitation energy transfer. A key question of the structure-function relationships in photosynthetic antennae is: How does the protein environment influence the optical transition energies of the pigments? Besides static and dynamic disorder caused by slow and fast protein dynamics, respectively, there is a specific change of the transition energy of every pigment due to the different protein environment. Different pigment-protein interactions are assumed to influence the optical transition energies of the pigments:

1. Electrostatic interactions with charged and aromatic amino-acid side chains (1,2).
2. Differences in Mg^{2+}-ligation (3).
3. Differences in H-bonding (4–7).
4. Differences in the conformation of the pigment; for example, the degree of planarity and the rotation angle of the acetyl group (8,9).

A direct calculation of transition energies of pigments in the protein, the so-called site energies, is difficult (2,9) because of the complexity of the above interactions. Therefore, the site energies are often treated as parameters that are determined from the fit of optical spectra.

There is one pigment-protein complex, the so-called Fenna-Matthews-Olson (FMO) complex of green sulfur bacteria, which has been extensively used as a model system for larger antenna complexes, starting more than 25 years ago with the pioneering work of Pearlstein (10) and co-workers. The FMO complex of Prosthecochloris aestuarii was the first pigment-protein complex for which the structure was determined by x-ray crystallography (11,12). In the meantime, the resolution of the electron density map has been refined to 1.9 Å (13) and the structure of the FMO complex of a strongly related bacterium Chlorobium tepidum has been determined as well (14,15). The two structures are very similar, but interestingly, the spectra look different. The molecular origin of this difference is unknown; an explanation is suggested in this study. The structure of the FMO complex consists of a trimer, formed by three identical monomers that each bind seven bacteriochlorophyll-a (BChla) molecules, as shown in Fig. 1. The usual numbering of the BChls (original chosen by Fenna and Matthews (11)) is used throughout this article.

The FMO trimer mediates excitation energy transfer between the chlorosomes, which are the main light-harvesting antennae of green sulfur bacteria and the membrane-embedded type I reaction center (RC) (16). There is some structural information on the FMO-RC super complex, obtained in an electron microscopic study (17,18) and from linear dichroism (LD) spectra measured on FMO trimers and FMO-RC complexes. The latter provide evidence that the symmetry axis of the trimer is parallel to the normal of the membrane, containing the reaction center and the former gave the overall
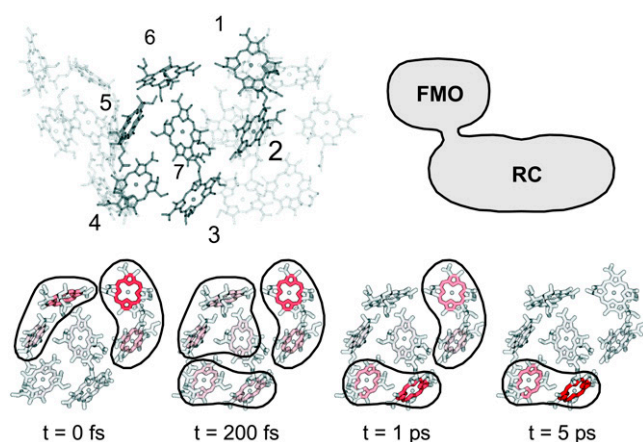
FIGURE 1 (*Left, top*) BChls of the FMO trimer. The BChls 1–7 of one monomeric subunit are highlighted (numbering according to Fenna and Matthews (11)). (*Right, top*) Sketch of the mutual arrangement of the FMO complex and the reaction center, as obtained from an electron-microscopic study (17,18). (*Bottom*) Spatial and temporal relaxation of excitons from the top to the bottom of the complex. As initial condition the exciton states with large contributions from BChls 1 and 6 were populated. The color of the π-system of the BChls is varied between light and dark red according to the population of the excited states. The enclosed areas mark the delocalized exciton states that are populated (see also Fig. 14).

mutual arrangement of the two complexes as sketched in the upper-right corner in Fig. 1. The resolution of the electron microscopic study does not allow us to distinguish between the top and the bottom of the FMO trimer. Hence, either BChls 1 and 6 or BChls 3 and 4 are the linker pigments between the FMO complex and the RC. Since the RC represents an energetic sink, it can be assumed that the low energy pigments serve as linkers.

Different sets of site energies of the seven BChla molecules have been extracted in the past from calculations of optical spectra (19–25), using different fit algorithms or simply by hand. The different calculations predict different pigments to be responsible for the lowest exciton state. The early exciton calculations by Pearlstein (19) suggested BChl 7; the calculations by Gülen (21) found the lowest site energy for BChl 6, and the calculations of Louwe et al. (22), Vulto et al. (24), Renger and May (23), and Wendling et al. (25) favor BChl 3. Based on the finding that the surface of the FMO trimer is more hydrophobic on the site of BChl 6 it was suggested that the FMO trimer is partially embedded in the membrane (14), a suggestion that would favor BChl 6 to be the linker between the FMO trimer and the reaction center. However, from the electron microscopy study on FMO-RC complexes, it was seen that the FMO complex is not part of the membrane (17,18), leaving again both options for the lowest energy pigment open. In the present study, two independent methods for the calculation of site energies provide compelling evidence that BChls 3 and 4 dominate the lowest exciton state and, for efficient excitation energy transfer to the reaction center, are the linker pigments. The temporal and spatial relaxation of excitons through the FMO

complex toward the RC that results from the site energies determined in this study is shown in the lower part of Fig. 1 and will be explained and discussed in detail later.

Until now, the best agreement between calculated and experimental optical spectra of the FMO complex has been obtained by Vulto et al. (22,24) for *C. tepidum* and by Wendling et al. (25) for *P. aestuarii*. In both cases BChl 3 was identified as the one with the lowest site energy. The crucial point of those studies (22,24,25) was the use of a smaller dipole strength of BChla (22) in the calculations of the excitonic couplings than assumed previously. A physical explanation of the rather small couplings is still missing and will be given here. Concerning the calculations of Vulto et al. (24) it was not clear whether the values for the site energies would change if a better theory for optical spectra were used, since lifetime broadening, vibrational sidebands, and resonance energy transfer narrowing of the optical lines were neglected (24). It is shown here that this rather harsh approximation does not lead to drastic changes in the relative shifts in optimized site energies. However, the quality of the fit of the spectrum is better if a more advanced theory of optical spectra (26) is used.

Insights into the dynamics of excitons in the FMO-complex are obtained from time-resolved nonlinear optical spectroscopy (27–32), which detected subpicosecond as well as picosecond exciton relaxation times. In contrast to pump-probe studies, the newly developed two-dimensional photon-echo technique (31,32) allows one to directly detect the coupling between different exciton levels and the energies of exciton states, and to infer from those quantities the spatial and temporal relaxation of excitons. However, such a structural interpretation still requires knowledge of the site energies and excitonic couplings of the pigments. In the recent analysis of the photon-echo data of the FMO complex (31, 32), the couplings of Vulto et al. (24) were used, with one exception—the excitonic coupling between BChl 5 and 6 was reduced from 94 cm^{-1} to 40 cm^{-1}. The site energies by Vulto et al. (24) were readjusted to fit the linear absorption and two-dimensional photon-echo spectra (31,32). In this study, we are aiming at a direct calculation of the excitonic couplings and the site energies.

There is just one study on the FMO complex that tried to obtain the relative shift of site energies directly, from semiempirical quantum chemical calculations (9). Different factors as nonplanarity of the BChl, rotation of the acetyl group, and charged amino acids (all charged amino acids within 5.5 Å of the pigments were taken into account) were identified, but no optical spectra were calculated. The overall spread of the site energy values (9) is too large by a factor of 2–5, judging by the width of the experimental spectra (25). We find that, even when the site energy differences are downscaled, the agreement between the calculated and experimental spectra is rather poor.

The article is organized in the following way. The theory used for the calculation of optical spectra and exciton

relaxation is summarized first. Next, the effect of the dielectric medium of the protein on the excitonic couplings of the pigments is investigated by electrostatic calculations. Afterwards, the site energies of the pigments are obtained by a fit of optical spectra, using a genetic algorithm and, independently, by the calculation of electrochromic shifts due to charged amino acids. The site energies and excitonic couplings are then used to calculate the temporal and spatial relaxation of excitons after a short pulse excitation or assuming that excitation energy arrives from the direction where the chlorosomes are situated in green sulfur bacteria.

THEORY

Hamiltonian

The theory is based on a standard Hamiltonian H_{ppc} for the pigment protein complex, that describes the pigments as coupled two-level systems interacting with vibrational degrees of freedom of the pigments and the protein,

$$H_{ppc} = H_{ex} + H_{ex-vib} + H_{vib}. \qquad (1)$$

The exciton part,

$$H_{ex} = \sum_m E_m |m\rangle\langle m| + \sum_{m \neq n} V_{mn} |m\rangle\langle n|, \qquad (2)$$

contains the site energies E_m of the pigments, defined as the optical transition energies at the equilibrium position of nuclei in the electronic ground state, and the excitation energy transfer couplings V_{mn}.

The Hamiltonian H_{ex-vib} describes the modulation of site energies by the vibrations. A linear dependence of the site energies on the (dimensionless) vibrational coordinate Q_ξ is assumed, which is defined in terms of creation and annihilation operators of vibrational quanta, $Q_\xi = C_\xi^\dagger + C_\xi$ (26,33):

$$H_{ex-vib} = \sum_\xi \sum_m \hbar\omega_\xi g_\xi^{(m)} Q_\xi |m\rangle\langle m|. \qquad (3)$$

The dimensionless coupling constants $g_\xi^{(m)} = g_\xi$ enter the spectral density $J(\omega)$ of the exciton vibrational coupling

$$J(\omega) = \sum_\xi g_\xi^2 \delta(\omega - \omega_\xi), \qquad (4)$$

which is the key quantity in the expressions for optical spectra and the rate constants for exciton relaxation discussed below. The value $J(\omega)$ is assumed independent on the site index m; i.e., the same local modulation of site energies by the vibrational dynamics is assumed.

The vibrations are described by an Hamiltonian H_{vib} of harmonic oscillators

$$H_{vib} = \sum_\xi \frac{\hbar\omega_\xi}{4} Q_\xi^2 + T_{nucl}, \qquad (5)$$

where T_{nucl} is the kinetic energy of nuclei.

The coupling between the pigment-protein complex and an external radiation field is described by the semiclassical Hamiltonian $H_{ppc-rad}$, which reads in rotating wave approximation

$$H_{ppc-rad} = -\sum_m \vec{\mu}_m \vec{e} E_\Omega(t) e^{-i\Omega t} |m\rangle\langle 0| + h.c., \qquad (6)$$

where $\vec{\mu}_m$ is the molecular transition dipole moment of the mth pigment, $\vec{e}$ the polarization of the field, and $h.c.$ the Hermitian conjugate. The field may be either stationary, i.e., $E_\Omega(t) = E_0$, or time-dependent. In the latter case, a Gaussian shape for $E_\Omega(t)$ is assumed as

$$E_\Omega(t) = \frac{E_0}{\sqrt{2\pi}\tau_p} e^{-t^2/(2\tau_p^2)}, \qquad (7)$$

where the full width at half-maximum (FWHM) of $E_\Omega(t)$ is $2\tau_p\sqrt{2\ln2}$.

For the calculations of optical spectra and exciton relaxation, the above Hamiltonian $H_{ppc} + H_{ppc-rad}$ is expressed in terms of delocalized exciton states $|M\rangle$, which are given as linear combinations of localized excited states $|M\rangle = \sum_m c_m^{(M)} |m\rangle$, where $|c_m^{(M)}|^2$ describes the probability that the mth pigment is excited when the PPC is in the Mth exciton state. The exciton coefficients $c_m^{(M)}$ and excitation energies ε_M are obtained from the solution of the eigenvalue problem

$$H_{ex} |M\rangle = \varepsilon_M |M\rangle, \qquad (8)$$

with the H_{ex} in Eq. 2. The Hamiltonian H_{ex-vib} in Eq. 3, in the basis of delocalized exciton states, becomes

$$H_{ex-vib} = \sum_{MN} \sum_\xi \hbar\omega_\xi g_\xi(M,N) Q_\xi |M\rangle\langle N|, \qquad (9)$$

with the coupling constant

$$g_\xi(M,N) = \sum_m c_m^{(M)} c_m^{(N)} g_\xi^{(m)}, \qquad (10)$$

that contains now diagonal ($M = N$) as well as off-diagonal ($M \neq N$) parts. The former give rise to vibrational sidebands of exciton transitions in optical spectra and the latter lead to relaxation between different exciton states.

The coupling to the radiation field $H_{ppc-rad}$ in Eq. 6 now reads

$$H_{ppc-rad} = -\sum_M \vec{\mu}_M \vec{e} E_\Omega(t) e^{-i\Omega t} |M\rangle\langle 0| + h.c., \qquad (11)$$

where the transition dipole moments $\vec{\mu}_M$ of the delocalized exciton states are obtained from the local transition dipole moments $\vec{\mu}_m$ and the exciton coefficients $c_m^{(M)}$ as

$$\vec{\mu}_M = \sum_m c_m^{(M)} \vec{\mu}_m. \qquad (12)$$

The above Hamiltonians lead to the expressions for linear optical spectra, exciton state occupation probabilities, created by a short pulse, and rate constants of exciton relaxation, described in the following.

Linear optical spectra

The linear absorption $\alpha(\omega)$ is obtained from the dipole-dipole correlation function as explained in detail in Renger and Marcus (26),

$$\alpha(\omega) \propto \left\langle \sum_M |\vec{\mu}_M|^2 D_M(\omega) \right\rangle_{\text{dis}}, \qquad (13)$$

where $D_M(\omega)$ is the lineshape function and $\langle \ \rangle_{\text{dis}}$ denotes an average over static disorder in site energies. A Gaussian distribution function of width (FWHM) Δ_{dis} is assumed for these energies, and the disorder average is performed by a Monte Carlo method. In the calculation of circular dichroism, the dipole strength $|\vec{\mu}_M|^2$ in Eq. 13 is replaced by the rotational strength r_M and in the case of linear dichroism by $|\vec{\mu}_M|^2(1 - 3\cos^2\theta_M)$, where θ_M is the angle between the symmetry axis of the trimer and the excitonic transition dipole moment $\vec{\mu}_M$.

The lineshape function $D_M(\omega)$ was obtained using a non-Markovian partial-ordering prescription theory. It is given as (26)

$$D_M(\omega) = \Re \int_0^\infty dt \, e^{i(\omega - \tilde{\omega}_M)t} \, e^{G_M(t) - G_M(0)} \, e^{-t/\tau_M}, \qquad (14)$$

where $\Re$ denotes the real part of the integral. The value $D_M(\omega)$ contains both vibrational sidebands and lifetime broadening due to exciton relaxation. The vibrational sidebands are described by $G_M(t)$ and the lifetime broadening by the dephasing time τ_M (discussed in detail below). Both quantities are related to the spectral density $J(\omega)$ in Eq. 4. The time-dependent function $G_M(t)$ in Eq. 14 is given as

$$G_M(t) = \gamma_{MM} G(t), \qquad (15)$$

with

$$G(t) = \int_0^\infty d\omega \left[(1 + n(\omega))J(\omega)e^{-i\omega t} + n(\omega)J(\omega)e^{i\omega t} \right] \quad (16)$$

and γ_{MM} being the diagonal part of

$$\gamma_{MN} = \sum_{m,n} e^{-R_{mn}/R_c} c_m^{(M)} c_m^{(N)} c_n^{(M)} c_n^{(N)}. \qquad (17)$$

It contains the exciton coefficients $c_m^{(M)}$, a correlation radius R_c of protein vibrations (26) (note that a value of $R_c = 5$ Å is used, determined from transient spectra of Photosystem II reaction centers in (34); the stationary spectra calculated here do not depend critically on this value) and the center-to-center distance R_{mn} between pigments m and n.

The function $n(\omega)$ in Eq. 16 is the mean number of vibrational quanta with energy $\hbar\omega$ that are excited at a given temperature T,

$$n(\omega) = \frac{1}{e^{\hbar\omega/kT} - 1}, \qquad (18)$$

where k is Boltzmann's constant. The dephasing time τ_M in Eq. 14 is determined by the rate constants $k_{M \to N}$ of exciton relaxation, obtained using a Markov approximation for the off-diagonal parts of the exciton vibrational coupling,

$$\tau_M^{-1} = \frac{1}{2} \sum_{N \neq M} k_{M \to N}, \qquad (19)$$

where the rate constant reads

$$k_{M \to N} = 2 \gamma_{MN} \tilde{C}^{(\text{Re})}(\omega_{MN}). \qquad (20)$$

It resembles the standard Redfield rate constant (e.g., (35)). The $\tilde{C}^{(\text{Re})}(\omega_{MN})$ is the real part of the Fourier-Laplace transform of the pigment's optical energy gap correlation function (26),

$$\tilde{C}^{(\text{Re})}(\omega_{MN}) = \pi \omega_{MN}^2 [(1 + n(\omega_{MN}))J(\omega_{MN}) + n(\omega_{NM})J(\omega_{NM})], \qquad (21)$$

where $J(\omega) = 0$ for $\omega < 0$, and $\omega_{MN} = \omega_M - \omega_N$ is the transition frequency between the Mth and the Nth exciton states. The $\tilde{\omega}_M$ in Eq. 14 is shifted from the purely electronic transition frequency ω_M due to the exciton-vibrational coupling

$$\tilde{\omega}_M = \omega_M + \sum_N \gamma_{MN} \tilde{C}^{(\text{Im})}(\omega_{MN})$$

$$= \omega_M - \gamma_{MM} \frac{E_\lambda}{\hbar} + \sum_{N \neq M} \gamma_{MN} \tilde{C}^{(\text{Im})}(\omega_{MN}), \qquad (22)$$

where γ_{MN} is given in Eq. 17 and E_λ is the local reorganization energy

$$E_\lambda = \hbar \int_0^\infty d\omega \, \omega J(\omega). \qquad (23)$$

The $\tilde{C}^{(\text{Im})}(\omega_{MN})$ in Eq. 22 is related to the real part $\tilde{C}^{(\text{Re})}(\omega)$ in Eq. 21 by a Kramers Kronig relation (26,36)

$$\tilde{C}^{(\text{Im})}(\omega_{MN}) = \frac{1}{\pi} \wp \int_{-\infty}^{+\infty} d\omega \frac{\tilde{C}^{(\text{Re})}(\omega)}{\omega_{MN} - \omega}, \qquad (24)$$

where $\wp$ denotes the principal part of the integral (details are given in the Supplementary Material).

In the present model, the spectral density $J(\omega)$ contains both a broad low frequency contribution $S_0 J_0(\omega)$ by the protein vibrations with Huang-Rhys factor S_0 and a single effective high-energy vibrational mode of the pigments with Huang-Rhys factor S_H:

$$J(\omega) = S_0 J_0(\omega) + S_H \delta(\omega - \omega_H). \qquad (25)$$

For the normalized low-frequency function $J_0(\omega)$ (with $\int_0^\infty J_0(\omega) \, d\omega = 1$), we assume that it has the same form as the spectral density, extracted recently (26) from 1.6 K fluorescence line narrowing spectra of B777-complexes,

$$J_0(\omega) = \frac{1}{s_1 + s_2} \sum_{i=1,2} \frac{s_i}{7! 2 \omega_i^4} \omega^3 \, e^{-(\omega/\omega_i)^{1/2}}, \qquad (26)$$

with the extracted parameters $s_1 = 0.8$, $s_2 = 0.5$, $\hbar\omega_1 = 0.069$ meV, and $\hbar\omega_2 = 0.24$ meV. The Huang-Rhys factor

S_0 of the pigment-protein coupling in Eq. 25 was estimated from the temperature dependence of the absorption spectra (28,37) of the FMO complexes of *P. aestuarii* and *C. tepidum* to be ~ 0.5. A comparison of the function $J_0(\omega)$ with the fluorescence line narrowing spectrum of *C. tepidum* (37) is shown at the top of Fig. 2. The experimental spectrum (for the present weak exciton-vibrational coupling) should be similar (26) to the $J(\omega)$ in Eq. 25. On the basis of this comparison, the Huang-Rhys factor and the energy of the high-frequency mode were estimated as $S_H = 0.22$ and $\omega_H = 180\,\text{cm}^{-1}$. By taking into account that the energy of the high-frequency mode is large compared to the thermal energy (at $T = 5$ K), i.e., $\hbar\omega_H \gg kT$, the function $G_M(t)$ in Eq. 15 becomes, using Eqs. 16 and 25,

$$G_M(t) = \gamma_{MM}\left(S_0 \int_0^\infty d\omega[(1 + n(\omega))J_0(\omega)e^{-i\omega t}\right.$$
$$\left. + n(\omega)J_0(\omega)e^{i\omega t}] + S_H e^{-i\omega_H t} \right)$$
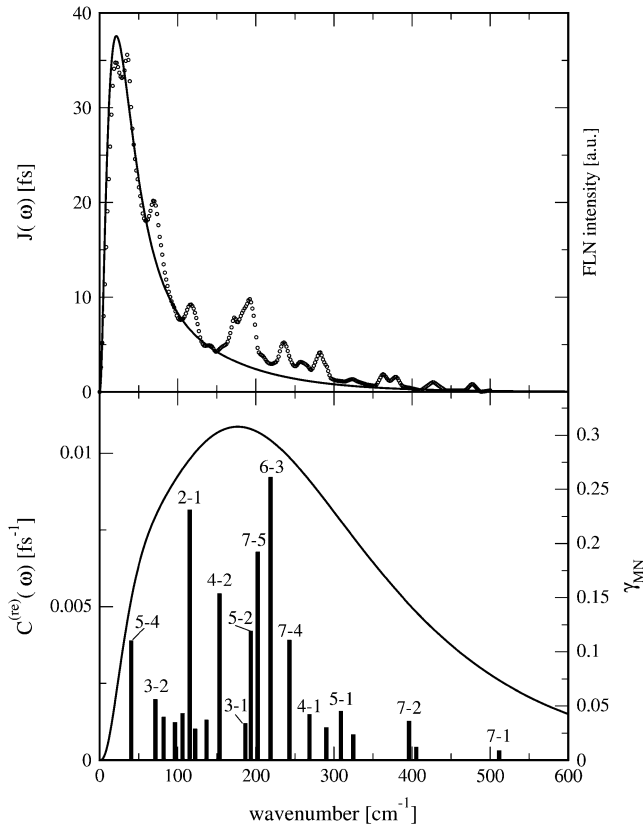$$= G_M^{(0)}(t) + \gamma_{MM}S_H e^{-i\omega_H t}. \tag{27}$$

FIGURE 2 (*Top*) Comparison of the low-frequency part $S_0 J_0(\omega)$ of the spectral density and the fluorescence line narrowing spectrum of *C. tepidum* (37). (*Bottom*) The function $\tilde{C}^{(\text{Re})}(\omega)$ is shown that results from the $S_0 J_0(\omega)$ at the top of this figure (Eq. 21). The factors γ_{MN} are shown as bars centered at the mean transition energy $\hbar\omega_{MN}$ between the exciton states. The numbers at the top of the bars show *M–N*.

By introducing this $G_M(t)$ into Eq. 14, using a series expansion for $\exp(\gamma_{MM}S_H e^{-i\omega_H t})$, the following lineshape function $D_M(\omega)$ is obtained:

$$D_M(\omega) = e^{-S_H\gamma_{MM}} \Re \int_0^\infty dt \sum_{k=0}^\infty \frac{(\gamma_{MM}S_H)^k}{k!}$$
$$\times e^{i(\omega - (\tilde{\omega}_M + k\omega_H))t} e^{G_M^{(0)}(t) - G_M^{(0)}(0)} e^{-t/\tau_M}. \tag{28}$$

The above $D_M(\omega)$ differs from the one obtained previously (26) in that it includes now also vibrational satellites of a high-frequency vibrational mode. The dephasing time τ_M of the *M*th exciton transition and the off-diagonal part of the shift in transition energy $\sum_{N\neq M}\gamma_{MN}\tilde{C}^{(\text{Im})}(\omega_{MN})$ in Eq. 22 are determined by the low frequency contribution $S_0 J_0(\omega)$ of the spectral density.

Relation of the present theory to the earlier theories by Vulto et al. (24) and Wendling et al. (25)

The theory used by Vulto et al. (24) is obtained from Eq. 13 by neglecting any homogeneous broadening, i.e., lifetime broadening and vibrational sidebands, by setting $G_M(t) = 0$ and $\tau_M^{-1} = 0$ in Eq. 14. In this case, the line-shape function $D_M(\omega)$ becomes just a delta-function that peaks at the exciton transition frequency ω_M, $D_M(\omega) = \delta(\omega - \omega_M)$. To perform the average over disorder analytically, any resonance energy transfer narrowing (38), i.e., a decrease of the width of the distribution of exciton energies with respect to that of the distribution of local transition energies, is neglected as well. Assuming a Gaussian distribution function $P(\omega_M - \bar{\omega}_M) = 1/\sqrt{2\pi\sigma^2}\,\exp[-(\omega_M - \bar{\omega}_M)^2/(2\sigma^2)]$ of the same width (FWHM) $2\sqrt{2\ln2}\,\sigma$ for all exciton energies $\hbar\omega_M$ results in

$$\alpha(\omega) \propto \frac{1}{\sqrt{2\pi\sigma^2}}\sum_M |\vec{\mu}_M|^2 e^{-(\omega - \bar{\omega}_M)^2/(2\sigma^2)}. \tag{29}$$

The mean exciton energies $\bar{\omega}_M$ are those obtained for the mean site energies.

In the theory of Wendling et al. (25,37), resonance energy transfer narrowing, lifetime broadening, and vibrational sidebands were taken into account using the following approximations for the function $D_M(\omega)$ in Eq. 14:

1. A shift of the transition frequency ω_M by the exciton vibrational coupling was neglected, i.e., $\tilde{\omega}_M = \omega_M$ in Eq. 22.
2. Any dependence of the vibrational sidebands of the exciton transitions on the delocalization of exciton states was neglected by replacing the function $G_M(t) = \gamma_{MM}G(t)$ in Eq. 14 by the function $G(t)$, which describes the vibrational sidebands of a monomeric BChla in a protein environment.
3. The factor $\pi\omega_{MN}^2$ appearing in Eqs. 19 and 21 for the rate constant of exciton relaxation between the *M*th and the *N*th state was approximated by a constant γ_0, which is assumed the same for all transitions $M \to N$, i.e., instead of the $\tilde{C}^{\text{Re}}(\omega)$ in Fig. 2 (*bottom*), a scaled $J(\omega)$ at the top of this figure is used.

The main differences between the present and the two earlier theories are illustrated in Fig. 3. Due to the neglect of vibrational sidebands in the theory of Vulto et al. (24) (*dotted line*), there is less intensity in the blue part of the spectrum. The missing lifetime broadening seems to be compensated in part by the neglect of resonance energy transfer narrowing as seen by the width of the two main peaks. In the theory of Wendling et al. (25,37), the neglect of the dependence of the vibrational sideband on the exciton states delocalization leads to a stronger vibrational sideband as seen in the blue part of the spectrum and to a change of the relative height of the two main peaks. We note that the differences between the three theories are partly compensated in the fit of optical spectra by different site energies. However, as will be seen below, the overall ranking of optimal site energies is similar in all three approaches.

Excitation by a short laser pulse

The Hamiltonian H_{ppc} in Eqs. 1–11 is rewritten, using the completeness relation, $|0\rangle\langle 0| + \sum_M |M\rangle\langle M| = 1$, as

$$H_{PPC} = U_0(Q)|0\rangle\langle 0| + \sum_M (\hbar\omega'_M + U_M(Q))|M\rangle\langle M|$$

where the diagonal part of the exciton-vibrational coupling was used to construct potential energy surfaces (PES) of exciton states

$$U_M(Q) = \sum_\xi \frac{\hbar\omega_\xi}{4}(Q_\xi + 2g_\xi(M,M))^2 \quad (31)$$
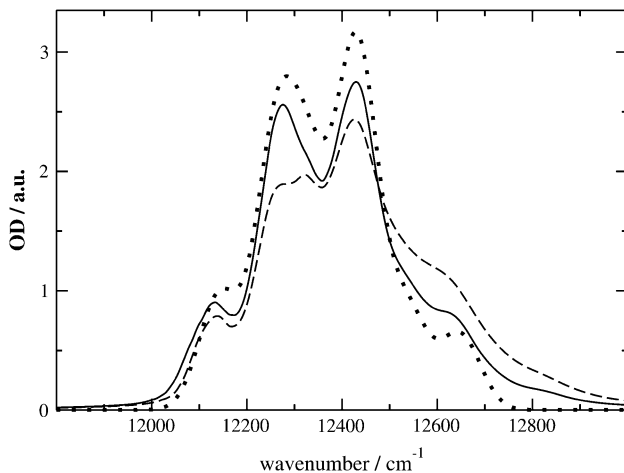

FIGURE 3 Calculation of absorption spectra of FMO-trimer of *C. tepidum* using site energy values from Table 4 and three different theories of optical spectra as explained in the text. The solid line shows the present theory; the dotted line shows Gauss-dressed stick spectra as in Vulto et al. (24); and the dashed line shows a theory in which the vibrational sidebands of exciton transitions were approximated by a vibrational sideband of monomeric BChl as in Wendling et al. (25). For better comparison, the dashed line was red-shifted by 50 cm^{-1} and the dotted line by 35 cm^{-1}.

that are shifted along the coordinate axis by $-2g_\xi(M,M)$ with respect to the PES $U_0(Q)$ of the ground state

$$U_0(Q) = \sum_\xi \frac{\hbar\omega_\xi}{4}Q_\xi^2. \quad (32)$$

The energy $\hbar\omega'_M$ is the transition energy between the minima of the excited state and the ground state PES,

$$\hbar\omega'_M = \hbar\omega_M - \gamma_{MM}E_\lambda, \quad (33)$$

where $\hbar\omega_M$ is the vertical transition energy (site energy) and E_λ the local reorganization energy in Eq. 23. It is assumed that the off-diagonal parts of the exciton-vibrational coupling are weak enough that the exciton relaxation during the short excitation pulse can be neglected. In this case, a nonperturbative inclusion of the diagonal part of the exciton vibrational coupling and a second-order perturbation theory with respect to $H_{ppc-rad}$ in Eq. 11 yields for the population $P_M(t)$ of the Mth exciton state

$$P_M(t) = \frac{|\vec{\mu}_M|^2}{3\hbar^2}\int_{t_0}^t d\tau \int_{t_0}^\tau d\tau_1 e^{i(\Omega-\omega'_M)(\tau-\tau_1)}E_\Omega(\tau)E_\Omega(\tau_1)$$
$$\times \mathrm{Tr}_{vib}\left\{e^{-\frac{i}{\hbar}U_M(\tau-\tau_1)}e^{\frac{i}{\hbar}U_0(\tau-\tau_1)}W_0^{(eq)}\right\} + h.c., \quad (34)$$

where Tr_{vib} denotes a trace with respect to the vibrational degrees of freedom, and the vibrationally relaxed initial electronic ground state is described by the equilibrium statistical operator $W_0^{(eq)}$

$$W_0^{(eq)} = \frac{e^{-(U_0 + T_{nucl})/kT}}{\mathrm{Tr}_{vib}\left\{e^{-(U_0 + T_{nucl})/kT}\right\}}, \quad (35)$$

and an average over a random orientation of complexes with respect to the polarization of the external field was performed. By changing the integration variable $\tau - \tau_1 \rightarrow \tau_1$, and setting $t_0 \rightarrow -\infty$, the occupation probability is obtained as

$$P_M(t) = 2\frac{|\vec{\mu}_M|^2}{3\hbar^2}\Re \int_0^\infty d\tau_1 e^{i(\Omega-\omega'_M)\tau_1}f(t,\tau_1)g(\tau_1), \quad (36)$$

where $\Re$ denotes the real part and $f(t, \tau_1)$ is given as

$$f(t,\tau_1) = \int_{-\infty}^t d\tau E_\Omega(\tau)E_\Omega(\tau-\tau_1), \quad (37)$$

which for $t \rightarrow \infty$ becomes the autocorrelation function of the pulse. The function $g(\tau_1)$ contains the average over the vibrational degrees of freedom that is performed using a second-order cumulant expansion, which is exact for harmonic oscillators (33)

$$g(\tau_1) = \mathrm{Tr}_{vib}\left\{e^{-\frac{i}{\hbar}U_M(\tau_1)}e^{\frac{i}{\hbar}U_0(\tau_1)}W_0^{(eq)}\right\} = e^{G_M(\tau_1)-G_M(0)}, \quad (38)$$

with the $G_M(t = \tau_1)$ in Eqs. 15 and 16.

The population of exciton states after the action of the short pulse $P_M^{(p)}$ is obtained by formally setting $t \rightarrow \infty$ in Eq. 37. With the $E_\Omega(t)$ in Eq. 7, the population $P_M^{(p)}$ reads

$$P_M^{(p)} = \frac{|\vec{\mu}_M|^2}{3\hbar^2} \frac{E_0^2}{\sqrt{\pi}\tau_p} \Re \int_0^\infty d\tau\, e^{-i(\Omega - \omega'_M)\tau} e^{G_M(\tau) - G_M(0)} e^{-\tau^2/(4\tau_p^2)}.$$
(39)

This result will be used as an initial condition in the calculation of exciton relaxation, discussed in the following.

Exciton relaxation dynamics

Exciton relaxation is described by modified Redfield theory (39–42). It is assumed that before exciton relaxation between different delocalized states the nuclei relax in the respective excitonic PES. The rate constant $k_{M \to N}$ is obtained in second-order perturbation theory in the off-diagonal part of the exciton-vibrational coupling. In contrast to Redfield theory, which neglects nuclear reorganization effects that accompany exciton relaxation, in modified Redfield theory those effects are taken into account by a nonperturbative inclusion of the diagonal part of the exciton-vibrational coupling. Within the present harmonic oscillator model the rate constant is obtained as (41,42)

$$k_{M \to N} = \int_{-\infty}^\infty d\tau\, e^{i\omega_{MN}\tau} e^{\phi_{MN}(\tau) - \phi_{MN}(0)}$$
$$\times \left[\left(\frac{\lambda_{MN}}{\hbar} + G_{MN}(\tau) \right)^2 + F_{MN}(\tau) \right],$$
(40)

where the time-dependent functions

$$\phi_{MN}(t) = a_{MN}\,\phi_0(t)$$
(41)
$$G_{MN}(t) = b_{MN}\,\phi_1(t)$$
(42)
$$F_{MN}(t) = c_{MN}\,\phi_2(t)$$
(43)

are related to the spectral density $S_0 J_0(\omega)$ via the function $\phi_k(t)$, with $k = 0, 1, 2$,

$$\phi_k(t) = S_0 \int_{-\infty}^\infty d\omega\, e^{-i\omega t}(1 + n(\omega))\,\omega^k (J_0(\omega) - J_0(-\omega)).$$
(44)

The time-independent part in the integrand in Eq. 40, λ_{MN}, is

$$\lambda_{MN} = d_{MN} E_\lambda,$$
(45)

using the local reorganization energy E_λ in Eq. 23 with $J(\omega) = S_0 J_0(\omega)$. The coefficients a_{MN}, b_{MN}, c_{MN}, and d_{MN} in the above equations are given by the exciton coefficients and the correlation radius of protein vibrations as (42)

$$a_{MN} = \sum_{mn} ((c_m^{(M)})^2 (c_n^{(M)})^2 + (c_m^{(N)})^2 (c_n^{(N)})^2$$
$$- 2(c_m^{(M)})^2 (c_n^{(N)})^2) e^{-R_{mn}/R_c},$$
(46)

$$b_{MN} = \sum_{mn} ((c_m^{(M)})^2 - (c_m^{(N)})^2) c_n^{(M)} c_n^{(N)} e^{-R_{mn}/R_c},$$
(47)

$$c_{MN} = \sum_{mn} c_m^{(M)} c_m^{(N)} c_n^{(M)} c_n^{(N)} e^{-R_{mn}/R_c},$$
(48)

$$d_{MN} = \sum_{mn} ((c_m^{(M)})^2 + (c_m^{(N)})^2) c_n^{(M)} c_n^{(N)} e^{-R_{mn}/R_c}.$$
(49)

If the diagonal part of the exciton vibrational coupling, i.e., the mutual shift of excitonic PES surfaces, is neglected, Eq. 40 reduces to the Redfield result in Eq. 20: The only function in Eq. 40 that does not contain a diagonal part of the coupling is the $F_{MN}(t)$ in Eq. 43 (41). After setting the remaining functions to zero, Eq. 40 becomes $k_{M \to N} = \int_{-\infty}^\infty d\tau\, e^{i\omega_{MN}\tau} F_{MN}(\tau)$. If the $F_{MN}(t)$ in Eq. 43 is introduced and the integration over τ is carried out, the rate constant becomes $k_{M \to N} = 2\pi\gamma_{MN}\omega_{MN}^2(1 + n(\omega_{MN}))(J(\omega_{MN}) - J(\omega_{NM}))$. By noting that $-(1 + n(\omega_{MK})) = n(\omega_{KM})$, the equality of the above rate constant with the Redfield result in Eq. 20 is seen.

Exciton relaxation dynamics is described by the rate equations for the populations $P_M(t)$ of exciton states,

$$\frac{d}{dt} P_M(t) = - \sum_{N \neq M} (k_{M \to N} P_M(t) + k_{N \to M} P_N(t)),$$
(50)

with the initial populations $P_M(0) = P_M^{(p)}$ created by the short pulse (Eq. 39).

Alternatively, exciton states which are formed by the pigments at the top of the trimer in Fig. 1 will be populated at time zero to mimic excitation energy transfer as it occurs in vivo between the chlorosomes and the RC. For the rate constants $k_{M \to N}$ the modified Redfield result in Eq. 40 or the Redfield expression in Eq. 20 is used. In matrix form, Eq. 50 reads $d/dt\, \vec{P}(t) = -A\vec{P}(t)$, where the Mth element of $\vec{P}(t)$ is $P_M(t)$ and the kinetic matrix A contains in the diagonal the elements $A_{MM} = \sum_{N \neq M} k_{M \to N}$ and in the off-diagonal $A_{MN} = -k_{N \to M}$. The standard solution for $\vec{P}(t)$ is given as $\vec{P}(t) = \sum_i d_i \vec{c}_i e^{-\lambda_i t}$, where the λ_i and $\vec{c}_i$ are the eigenvalues and (right) eigenvectors of the kinetic matrix A and the constants d_i are obtained from the initial condition $\vec{P}(0) = \sum_i d_i \vec{c}_i$.

EXCITONIC COUPLINGS IN THE DIELECTRIC ENVIRONMENT OF THE PROTEIN

Although the excitonic couplings, in contrast to the site energies, can be calculated straightforwardly from the structural data, there is an unknown scaling factor that contains the uncertainty about the effect of the dielectric environment on the Coulomb (excitonic) interaction. In point dipole approximation, the excitonic coupling is given as

$$V_{mn} = f \frac{\mu_{\text{vac}}^2}{R_{mn}^3} [\vec{e}_m \cdot \vec{e}_n - 3(\vec{e}_m \cdot \vec{e}_{mn})(\vec{e}_n \cdot \vec{e}_{mn})],$$
(51)

where $\vec{e}_m$ is a unit vector along the transition dipole moment of the mth BChl, the unit vector $\vec{e}_{mn}$ is oriented along the line connecting the centers of BChls m and n, and μ_{vac}^2 is the dipole strength of the Q_y transition of BChla in vacuum. The factor f describes the enhancement of the dipole strength and the screening of the Coulomb coupling by the dielectric environment with optical dielectric constant ε,

$$f = g \frac{\mu(\varepsilon)^2}{\mu_{\text{vac}}^2}.$$
(52)

If the distance between the pigments is large compared to the extension of their ground and excited state wavefunctions, the screening factor g equals $1/\varepsilon$. If two pigments are very close, it can be expected that the factor f becomes distance-dependent, because the two pigments do not form separate cavities with dielectric medium in between, but are instead situated in the same cavity. As pointed out by Knox and van Amerongen (43), the enhancement of the dipole strength, i.e., the change in quantum mechanical transition probability by the dielectric, can be classically understood by the change of local electric field interacting with the vacuum transition dipole. Recently, Knox and Spring (44) analyzed the dipole strength of BChla in 15 different solvents and found the empirical relation $\mu(\varepsilon)^2 = (43.3 + 24.2 \, (\sqrt{\varepsilon} - 1)) \, D^2$ between the dipole strength $\mu(\varepsilon)^2$ in the solvent with dielectric constant ε and the vacuum value $\mu(1)^2$. If this empirical formula is compared with the predictions of two cavity models, the empty cavity model was found to provide the best explanation (44). Within the latter, the dipole strength of BChla in the solvent is obtained as $\mu(\varepsilon)^2 = 37.1 \, (3\varepsilon/(2\varepsilon + 1))^2 \, D^2$, that contains the vacuum dipole strength $\mu_{vac}^2 = \mu(1)^2 = 37.1 \, D^2$.

In a recent study, Hsu et al. (45) demonstrated that the excitonic coupling between two molecules in a dielectric environment, resulting from a quantum mechanical treatment with time-dependent density functional theory, can also be obtained classically. The classical calculation just involves the electrostatic coupling between the transition densities of the two molecules taking into account the fast (optical) part of the dielectric response of the medium. Hsu et al. (45) showed, using a multipole expansion, that the interaction between two transition dipoles in a spherical cavity can be either increased or decreased by the dielectric response of the environment, depending on the geometry of the transition dipoles.

As described in detail below, the present method is based on a numerical solution of the Poisson equation and allows us thereby to also treat nonspherical cavities, as those of the BChls in the FMO-protein. We have tested our numerical procedure by reproducing the spherical cavity results of Hsu et al. (45), as shown in Fig. 4. In this calculation, the transition dipoles are represented by two transition charges of opposite sign at close distance. The two geometries are depicted in Fig. 4 (left) and the resulting couplings are shown in Fig. 4 (right) in dependence on the dielectric constant.

In the following, we take into account nonspherical cavities of the BChls in the FMO-protein. The dielectric of the FMO-protein is generated by using overlapping spheres for its atoms, with atomic radii taken from the force field used by the program CHARMM (46), as illustrated in Fig. 5 (right). An optical dielectric constant of $\varepsilon = 2$ is assumed for the protein. The BChls are described by empty cavities that contain transition charges $\rho_m(\vec{r}) = \sum_I q_I \delta(\vec{r} - \vec{R}_I)$ describing the optical transition. The atomic transition monopole (TM) charges q_I of Chang (47) are placed at the position $\vec{R}_I$ of the atom I of the mth BChl. The charges were scaled so as to result in a vacuum transition dipole moment square of 37.1 D^2 of the empty cavity analysis by Knox and Spring (44). The excitonic couplings are obtained from the Coulomb interaction of the transition charges of different BChls. The respective vacuum results are shown in column (1) of Tables 1 and 2. To calculate the excitonic coupling between the BChls in the dielectric environment, the Poisson equation

$$\nabla \cdot [\varepsilon(\vec{r}) \nabla \phi_m(\vec{r})] = -4\pi \sum_I q_I \, \delta(\vec{r} - \vec{R}_I^{(m)}) \qquad (53)$$

is solved for each BChl numerically by a finite difference method using the program MEAD (48). The value of $\varepsilon(\vec{r})$ equals 2 if $\vec{r}$ points to a position in the protein and 1 in the case of BChl. From the resulting electrostatic potential $\phi_m(\vec{r})$
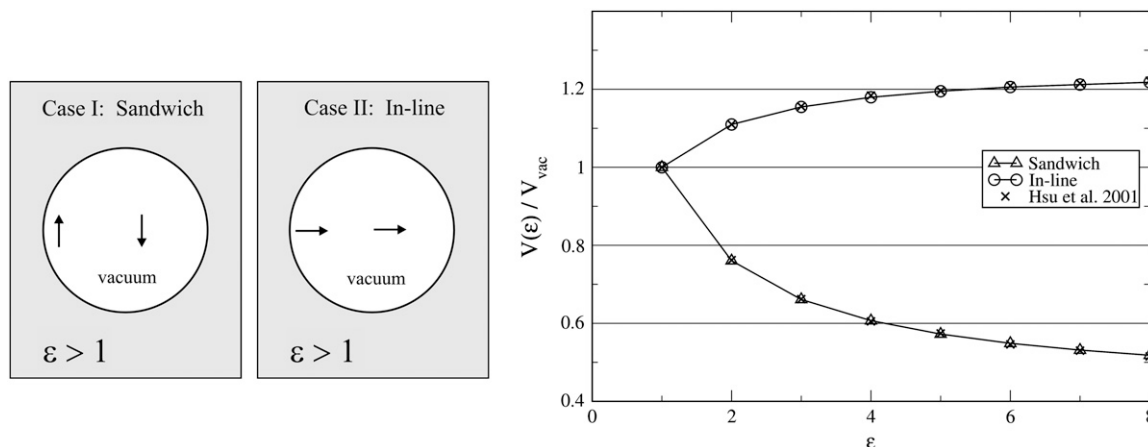

FIGURE 4 (Left) Sketch of the spherical cavity containing two transition dipoles with different geometries. The dipoles are located at $(-0.8,0,0)$ and $(0.1,0,0)$. The cavity radius equals 1. (Right) Ratio of the Coulomb coupling obtained for different dielectric constants ($\varepsilon > 1$) and the Coulomb coupling in vacuum ($\varepsilon = 1$) for the two geometries in the left panels. The values obtained earlier by Hsu et al. (45) using a multipole expansion are shown also.
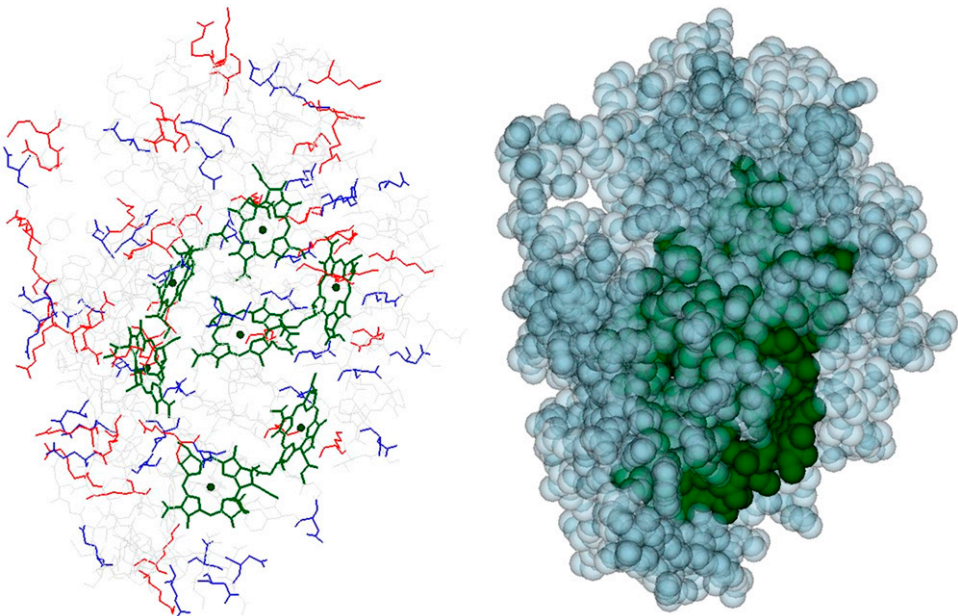
FIGURE 5 Structure of monomeric subunit of the FMO complex of *C. tepidum*. (*Left*) BChls are green; positively charged amino acids (Arg, Lys) are red; negatively charged amino acids (Asp, Glu) are blue; and neutral amino acids are gray. (*Right*) Dielectric volume used in the calculation of excitonic couplings. The protein (*gray*) forms a cavity around the BChls (*green*).

of BChl m, the excitonic coupling with BChl n is obtained as $V_{mn} = \int d\vec{r} \, \phi_m(\vec{r}) \, \rho_n(\vec{r}) = \sum_I \phi_m(\vec{R}_I^{(n)}) q_I$.

The results for the couplings (column (3) in Table 1 and 2) are compared to the values obtained for $\varepsilon = 1$ in the transition

monopole approximation (column (1)), and point dipole approximation from Eq. 51, using $f = 1.0$ (column (2)) and $f = 0.8$ (column (4)). A least mean-square fit, $V_{mn}^{TM}(\varepsilon = 2) = f \, V_{mn}^{TM}(\varepsilon = 1)$, for the transition monopole couplings in

TABLE 1 Excitonic couplings for *C. tepidum*

	(1) TM $\varepsilon = 1$	(2) Eq. 51, PD $f = 1$	(3) MEAD, TM $\varepsilon = 2$	(4) Eq. 51, PD $f = 0.8$
1-2	**−121.8**	**−109.6**	**−96.0**	**−87.7**
1-3	7.1	6.9	5.0	5.5
1-4	−7.5	−7.4	−4.4	−5.9
1-5	8.1	8.4	4.7	6.7
1-6	−16.8	−17.1	−12.6	−13.7
1-7	−9.6	−12.3	−6.2	−9.9
2-3	**39.1**	**38.5**	**33.1**	**30.8**
2-4	10.3	10.2	6.8	8.2
2-5	1.4	0.8	4.5	0.7
2-6	13.0	14.8	7.4	11.8
2-7	4.4	5.4	−0.3	4.3
3-4	**−73.4**	**−66.8**	**−51.1**	**−53.5**
3-5	−2.2	−2.7	0.8	−2.2
3-6	−11.7	−12.0	−8.4	−9.6
3-7	7.3	7.5	7.6	6.0
4-5	**−94.7**	**−88.4**	**−76.6**	**−70.7**
4-6	−20.6	−21.3	−14.2	−17.0
4-7	**−82.2**	**−79.1**	**−67.0**	**−63.3**
5-6	**95.3**	**101.4**	**78.3**	**81.1**
5-7	−2.8	−1.6	−0.1	−1.3
6-7	**48.5**	**49.6**	**38.3**	**39.7**

Expressed in units of cm^{-1}. Columns: (*1*) Transition monopole approximation using transition charges of Chang (47). (*2*) Point dipole approximation with $f = 1$ in Eq. 51. (*3*) Electrostatic calculation of transition monopole coupling in dielectric environment of the protein (with optical dielectric constant $\varepsilon = 2$) using the program MEAD and the same transition charges as for the calculations in column (*1*). (*4*) Point-dipole couplings, Eq. 51, obtained for $f = 0.8$. Large couplings are written in boldface.

TABLE 2 Excitonic couplings for *P. aestuarii*

	(1) TM $\varepsilon = 1$	(2) Eq. 51, PD $f = 1$	(3) MEAD, TM $\varepsilon = 2$	(4) Eq. 51, PD $f = 0.8$
1-2	**−133.0**	**−122.8**	**−104.1**	**−98.2**
1-3	6.9	6.7	5.1	5.4
1-4	−7.5	−7.4	−4.3	−5.9
1-5	8.5	8.9	4.7	7.1
1-6	−19.8	−19.1	−15.1	−15.2
1-7	−11.3	−16.9	−7.8	−13.5
2-3	**37.9**	**38.1**	**32.6**	**30.5**
2-4	10.4	9.9	7.1	7.9
2-5	2.0	1.8	5.4	1.4
2-6	15.0	16.4	8.3	13.1
2-7	5.8	10.6	0.8	8.5
3-4	**−69.1**	**−69.6**	**−46.8**	**−55.7**
3-5	−1.7	−2.3	1.0	−1.8
3-6	−11.3	−11.9	−8.1	−9.5
3-7	4.1	3.9	5.1	3.1
4-5	**−88.1**	**−82.1**	**−70.7**	**−65.7**
4-6	−21.7	−22.7	−14.7	−18.2
4-7	**−76.4**	**−72.7**	**−61.5**	**−58.2**
5-6	**109.2**	**111.1**	**89.7**	**88.9**
5-7	−5.9	−4.3	−2.5	−3.4
6-7	**40.9**	**45.6**	**32.7**	**36.5**

Expressed in units of cm^{-1}. Columns: (*1*) Transition monopole approximation using transition charges of Chang (47). (*2*) Point dipole approximation with $f = 1$ in Eq. 51. (*3*) Electrostatic calculation of transition monopole coupling in dielectric environment of the protein (with optical dielectric constant $\varepsilon = 2$) using the program MEAD and the same transition charges as for the calculations in column (*1*). (*4*) Point-dipole couplings, Eq. 51, obtained for $f = 0.8$. Large couplings are written in boldface.

columns (1) and (3) results in $f = 0.80$. The closest couplings between $V_{mn}^{TM}(\varepsilon = 2)$ and the point dipole approximation (column (2)) were obtained by using a factor of $f = 0.81$ (*P. aestuarii*) and 0.82 (*C. tepidum*), i.e., we obtain nearly the same correction factor as for the difference between $V_{mn}^{TM}(\varepsilon = 2)$ and $V_{mn}^{TM}(\varepsilon = 1)$. It is clear, thereby, that the point dipole approximation works well and that the main effect on the couplings is due to the dielectric environment. The present factor of 0.80–0.82 is somewhat larger than the factor 0.72 ($\varepsilon = 2$) obtained for point dipoles in a spherical cavity.

A closer examination, using extended dipoles instead of transition monopoles, shows that approximately half of the deviations occur because of the more realistic charge distribution and the remaining half due to the more realistic cavity shape and the fact that cavities of neighboring pigments overlap. However, overall, the simple spherical empty cavity model is seen to work surprisingly well, being off by just ~10%. In the calculation of optical spectra and exciton relaxation presented below we use the point dipole approximation and a factor $f = 0.8$ for both *P. aestuarii* and *C. tepidum*.

Finally, we note that the Knox/Spring analysis of the dipole strengths was limited to the 0–0 transition of the BChla Q_y transition, i.e., it does not include excitations of intramolecular vibrations. To take into account excitonic couplings that involve intramolecular vibrational transitions would require us to include those vibrational modes via the respective Franck Condon factors explicitly in the theory (see e.g. (49,50)), which is beyond the scope of this article. We have performed dimer calculations with and without an explicit vibrational transition to investigate whether, in a simple theory that does not take into account such a transition, the dipole strength of the latter should be included in the calculation of the excitonic coupling. From a comparison of the spectral position of the main peaks in the absorption spectrum obtained in the sophisticated and the simple theory, it is seen that, just taking into account the excitonic coupling that results from the 0-0 transition dipole strength, gives better results in the simple theory.

CALCULATION OF SITE ENERGIES

In the following, two independent methods are used to obtain the site energies of the seven BChla molecules of the monomeric subunits of the FMO complex of *P. aestuarii* and *C. tepidum*. First, the site energies are used as parameters that are optimized by a genetic algorithm in the fit of optical spectra. Afterwards, the site energies are obtained directly by electrochromic shift calculations.

Genetic algorithm

An often successful way to treat nonlinear multidimensional optimization problems is to use a genetic algorithm as a fit routine (51–53). A rough description of the optimization process is given in Fig. 6. In the initial step, N sets of site energies are generated (a so-called population of N chromosomes), one set is provided (start set), and $N - 1$ are randomly created. The corresponding spectra are calculated, and the different sets are ranked according to their fitness value, which is obtained from the reciprocal of the mean-square deviation between the calculated and experimental spectrum. To get better individuals from generation to generation, genetic operations (51,52) known as ''recombination'' and ''mutation'' (Fig. 7) are performed, taking the ranking into account. In each step, the chromosome with the highest rank is copied to the next cycle (reproduction). The fit is iteratively completed.

The algorithm was tested first by replacing the experimental spectrum by a calculated spectrum, shown as circles in Fig. 8, which was obtained for the site energies given in the last column (*True*) of Table 3. A simultaneous fit of the absorption (OD), linear dichroism (LD), circular dichroism (CD), and the derivative of the absorption (OD′) spectrum was performed. A typical population of 100 chromosomes was used. After 200 iteration steps, the values for the site energies found by the algorithm were within ± 2 cm^{-1} of the true values for convenient initial values and within ± 8 cm^{-1} for inconvenient initial values. The algorithm converges fast, if all initial values for the site energies are chosen equal at an energy of 12,460 cm^{-1} in the center of the target spectrum. The spectrum resulting for those initial site energies is shown as a dotted line in Fig. 8. The most difficult situation occurred with an inverted order of the initial values with respect to the optimal values. The respective initial spectrum is shown as a dashed line in Fig. 8. If the OD spectrum alone was fitted, the optimal site energies obtained were wrong, even if a population of 500 chromosomes was used.
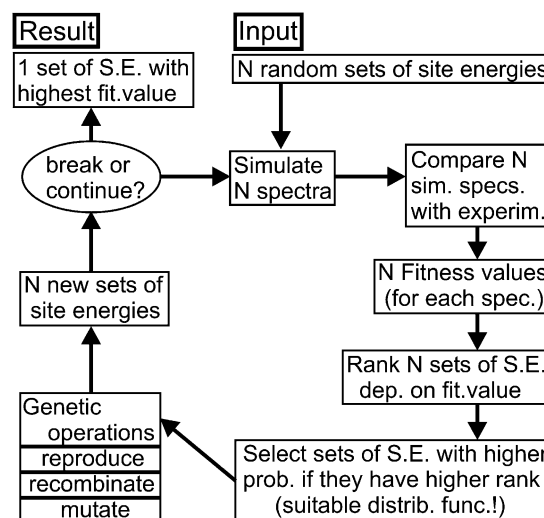

FIGURE 6   Working scheme of the genetic algorithm, as explained in the text.
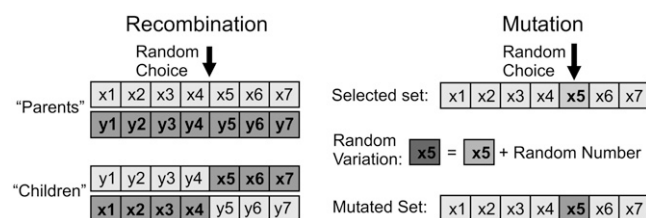
FIGURE 7 Genetic operations: Recombination and Mutation, as explained in the text.

Fit of low-temperature spectra of *C. tepidum and* P. *aestuarii*

The genetic algorithm was used for a simultaneous fit of the OD, OD′, CD, and LD spectra of *C. tepidum* and *P. aestuarii*, measured by Vulto et al. (24) and Wendling et al. (25). The temperature of measurement and simulation was 6 K for *C. tepidum* and 4 K for *P. aestuarii*. A width of 100 cm^{-1} for the distribution function of site energies gave the best agreement between the calculated and experimental spectra. The excitonic couplings in column (4) of Table 1 for *C. tepidum* and of Table 2 for *P. aestuarii* were used in the optimization. The fit of site energies was performed for the monomeric as well as for the trimeric structure of the FMO complex, to evaluate the effect of the intermonomer couplings. The optimal site energies obtained from the fits are shown in Table 4. As one can see, the maximum deviation of optimal site energies between monomer and trimer calculations is 70 cm^{-1} (BChl 7 of *P. aestuarii*), and the ranking of the site energies is almost identical. In accordance with some of the earlier results (24,25), pigment number 3 has the lowest site energy for *C. tepidum* and *P. aestuarii* and the largest deviation in site energies between the two species is obtained for BChl 5. The overall ranking in site energies
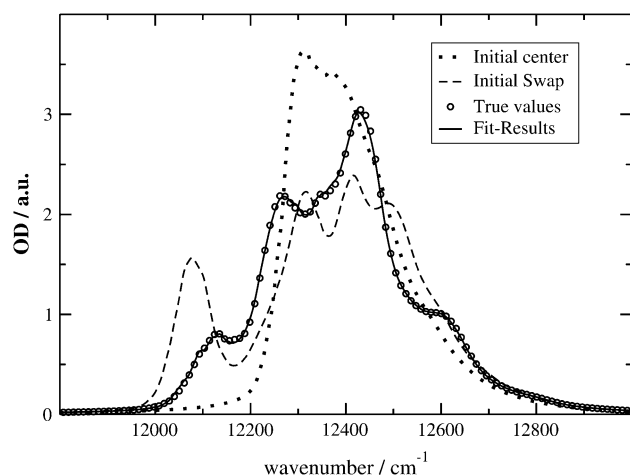

FIGURE 8 Test of the genetic algorithm. The two *Initial* spectra are obtained for different initial sets of site energies used in the genetic algorithm as explained in the text. The *True* spectrum is used in place of the experimental spectrum; it is obtained for a set of known test values of site energies. The *Fit-Results curve* (*solid line*) shows the spectra obtained for the two sets of optimal site energies given in Table 3.

TABLE 3 Test of the genetic algorithm

| | Initial | | Fit-Result | | |
BChl	Center	Swap	Center	Swap	True
1	12,460	12,450	12,451	12,442	12,450
2	12,460	12,470	12,521	12,514	12,520
3	12,460	12,550	12,210	12,207	12,210
4	12,460	12,540	12,320	12,317	12,320
5	12,460	12,210	12,548	12,558	12,550
6	12,460	12,320	12,542	12,538	12,540
7	12,460	12,520	12,471	12,469	12,470

All site energy expressed in units of cm^{-1}. The *True* values are site energies that were used to calculate a spectrum that is used instead of the experimental spectrum in the fit. The *Initial* values are different sets of initial site energies used in the fit, as explained in the text, and the *Fit-Result* values are the respective optimal site energies obtained from the genetic algorithm.

obtained here, is almost identical to those obtained earlier by Vulto et al. (24) and Wendling et al. (25) as seen in Table 4. The spectra obtained for the present optimal site energies for monomers and trimers are compared in Fig. 9 with the experimental data (24,25). Although the spectra for the monomers and the trimers are very similar, there are some quantitative differences for the CD spectrum of *P. aestuarii* that cannot be ignored. Hence, in the following, all calculations of optical spectra are done for the trimeric structure. The quality of the trimer fit is very good for all spectra of *C. tepidum* and for OD and LD of *P. aestuarii*, and somewhat weaker for CD of the latter.

Electrochromic shifts

For a microscopic interpretation of the site energies obtained above, electrochromic shifts in site energies due to charged amino acids are calculated in the following. The interaction between a charged amino acid and a pigment is described by $\hat{W} = -\hat{\mu} \cdot \vec{E}$, where $\hat{\mu}$ is the dipole operator of the pigment and $\vec{E}$ is the electric field created by the charge of the amino acid at the position of the pigment. In first order perturbation

TABLE 4 Site energies for *C. tepidum* and *P. aestuarii*

| | *C. tepidum* | | | *P. aestuarii* | | |
BChl	Monomer	Trimer	Vulto et al. (24)	Monomer	Trimer	Wendling et al. (25)
1	12,445 **3**	12,410 **3**	12,400 **3**	12,475 **5**	12,445 **3**	12,430 **4**
2	12,520 **6**	12,530 **6**	12,600 **7**	12,460 **4**	12,450 **4**	12,405 **3**
3	12,205 **1**	12,210 **1**	12,140 **1**	12,225 **1**	12,230 **1**	12,175 **1**
4	12,335 **2**	12,320 **2**	12,280 **2**	12,405 **2**	12,355 **2**	12,315 **2**
5	12,490 **5**	12,480 **5**	12,500 **5**	12,665 **7**	12,680 **7**	12,625 **7**
6	12,640 **7**	12,630 **7**	12,500 **6**	12,545 **6**	12,560 **6**	12,500 **6**
7	12,450 **4**	12,440 **4**	12,430 **4**	12,440 **3**	12,510 **5**	12,450 **5**

Expressed in units of cm^{-1}. Obtained from the fit of optical spectra in Fig. 9 for FMO-monomers and trimers, together with earlier fit results of Vulto et al. (24) and Wendling et al. (25). The bold numbers give the rank starting with the smallest site energy.
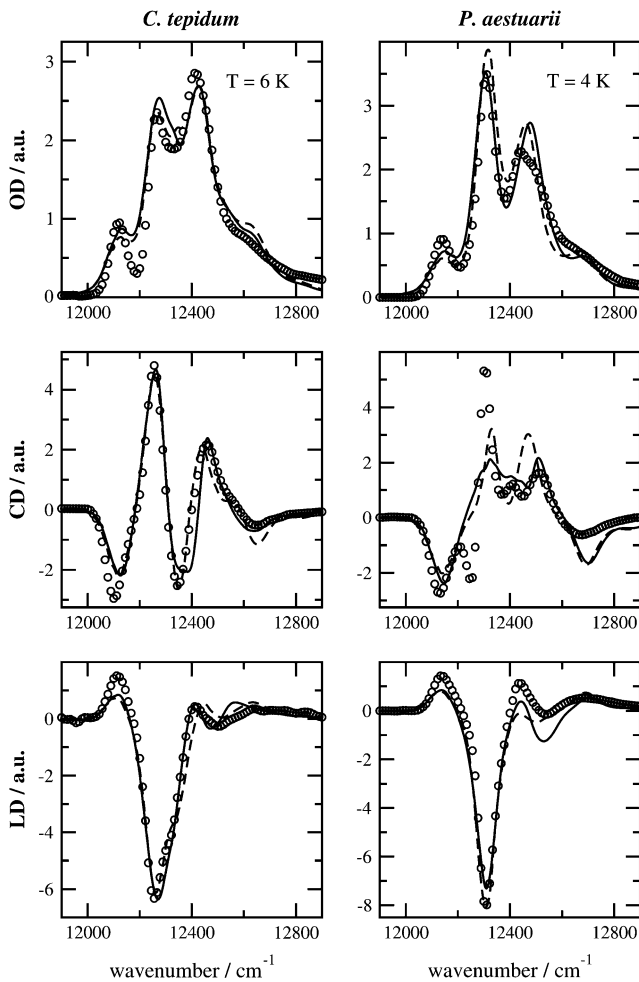
FIGURE 9 Low temperature optical spectra calculated for optimal site energies shown in Table 4. The top panels contain absorption (*OD*), the center panels contain circular dichroism (*CD*), and the bottom panels contain linear dichroism (*LD*) spectra. The experimental data of Vulto et al. (24) for *C. tepidum* (*left*) and of Wendling et al. (25) for *P. aestuarii* (*right*) are compared with monomer (*dashed lines*) and trimer (*solid lines*) calculations.

theory in $\hat{W}$ the shift in transition energy ΔE of the pigment is obtained as $\Delta E = \langle 1|\hat{W}|1\rangle - \langle 0|\hat{W}|0\rangle$, where $|0\rangle$ and $|1\rangle$ we are the ground and excited state of the pigment, respectivly.

We note that in second order perturbation theory in $\hat{W}$ an additional shift $-1/2\ \Delta\alpha\ E^2$ occurs, where $\Delta\alpha$ is the difference in polarizability of the two electronic states (54,55). Including the $\Delta\alpha$ reported for BChLa from Stark experiments (56), spectral band shift measurements in solution (57) and quantum chemical calculations (54) has a small effect on the calculated electrochromic shifts. The site energies obtained, including the $\Delta\alpha$-term, are within 10% of those obtained by neglecting this term. The large variance in the reported $\Delta\alpha$ values ranging from -4.3 Å^3 (54) to 16 Å^3 (57) makes it difficult to obtain a reliable estimate of the small correction term for the site energies. Therefore this second order correction is neglected in this study and

only the first order term described above is taken into account.

The shift ΔE_i of the transition energy of the ith pigment in a field of N point charges q_j in a dielectric medium then follows as

$$\Delta E_i = \frac{1}{\varepsilon_{\text{eff}}} \sum_{j=1}^{N} q_j \cdot \frac{\Delta\vec{\mu}_i \cdot \vec{r}_{ij}}{r_{ij}^3}, \tag{54}$$

where $\Delta\vec{\mu}_i = \vec{\mu}_{11}^i - \vec{\mu}_{00}^i$ is the difference of the permanent dipole moments of and ground excited-state of the ith pigment and $\vec{r}_{ij} = \vec{r}_j - \vec{r}_i$ is the vector connecting the center of the ith pigment with the jth point charge. The effective dielectric constant ε_{eff} in the denominator of Eq. 54 is used to describe the screening and local field effects by the dielectric environment (58) in an effective way. This method has been successfully applied to calculate electrochromic shifts of pigment transition energies due to oxidized and reduced pigments in bacterial reaction centers (58) and Photosystem II reaction centers (42). Here, the method is applied to calculate site energy shifts due to charged amino acids.

The experiments were performed at pH 8 (24,25). For simplicity, we assume that this pH value also applies to the environment of all the titratable groups in the protein and hence arginine (Arg) and lysine (Lys) are positively charged, whereas aspartic acid (Asp) and glutamic acid (Glu) carry a negative elementary charge. The charges were located at the center of charge of the amino acid, obtained from the atomic partial charges of the force field used by the program CHARMM (46,59).

The difference vector of excited- and ground-state permanent dipole moments $\Delta\vec{\mu}_i$ is assumed to be of equal magnitude and orientation with respect to the BChla macrocycle for all pigments. From Stark spectra of BChla (60), a value for $|\Delta\vec{\mu}|$ between 1.6 D and 2.4 D and an orientation of $\Delta\vec{\mu}$ approximately along the $N_B \rightarrow N_D$ axis of the BChl can be estimated (60). (Note that for BChla in polystyrene ($\varepsilon = 2.6$), a value $|\Delta\vec{\mu}|/f$ of 2–3 D was reported (60). Using the empty cavity factor $f = 3\varepsilon/(2\varepsilon + 1)$ then results in $|\Delta\vec{\mu}| = 1.6$–2.4 D) In the present calculations we use $|\Delta\vec{\mu}| = 2.0$ D and determine ε_{eff} from the fit of the overall width of the spectrum obtained for the calculated site energies. The site energy E_i for BChl i is given by

$$E_i = E_0 + \Delta E_i, \tag{55}$$

where the constant E_0 is assumed, first, to be equal for all pigments and will be determined from the overall spectral position of the spectrum and comparison with experiment. Later, the E_0 for the two pigments with nonhistidine ligands will be allowed to vary.

The electrochromic shifts ΔE_i calculated by Eq. 54 for *C. tepidum* and *P. aestuarii* are listed in Table 5. The strongest red-shift is obtained for BChl 3 for both species. The largest difference between the two species is obtained for BChl 5. Whereas the site energy of this pigment shifts to the red in

TABLE 5 Electrochromic shifts ΔE_i

| BChl i | $C.\ tepidum$ | | $P.\ aestuarii$ | |
	ΔE_i $\varepsilon_{\mathrm{eff}} = 3.8$	$E_0 + \Delta E_i$ $E_0 = 12{,}315$	ΔE_i $\varepsilon_{\mathrm{eff}} = 4.3$	$E_0 + \Delta E_i$ $E_0 = 12{,}350$
1	115	12,430	135	12485
2	−50	12,265	−15	12,335
3	−105	12,210	−135	12,215
4	120	12,435	105	12,455
5	−70	12,245	35	12,385
6	195	12,510	165	12,515
7	0	12,315	30	12,380

Electrochromic shifts ΔE_i (Eq. 54) and site energies $E_0 + \Delta E_i$ for $C.\ tepidum$ and $P.\ aestuarii$ expressed in units of cm^{-1}.

$C.\ tepidum$, it shifts to the blue in $P.\ aestuarii$. The main contributors to the red-shift of BChl 3 are Arg-32, Asp-260, Lys-30, Lys-34, and Lys-267 in $C.\ tepidum$ and their equivalents Arg-32, Asp-261, Lys-30, Lys-34, and Lys-268 in $P.\ aestuarii$. The situation is different for BChl 5, where the number of main contributors is much larger and the equivalence of the dominating charged amino acids is much less in the two species. A main contributor to the large blue-shift of BChl 6 is its positively charged hydrogen-bond donor Arg-95, which is conserved in both species and is responsible for one-third of the difference in site energies between BChl 3 and BChl 6. The specific contributions of each titratable group to the electrochromic shift of the different pigments is given in the Supplementary Material. The largest deviations between the fitted site energies in Table 4 and the values obtained from the electrochromic shift calculation in Table 5 are obtained for BChls 2 and 5, which are the only two pigments not ligated by histidine (His) but by a water bridge to Asn (BChl 2) and by Leu (BChl 5).

To take into account the influence of the different ligands on the site energy, a partial fit of the OD, OD′, LD, and CD spectra was performed using just the site energies of BChls 2 and 5 as fit parameters and applying the site energies obtained from the electrochromic shift calculations in Table 5 for the remaining five BChls. In case of BChl 5 which is

ligated by Leu in both species, $C.\ tepidum$ and $P.\ aestuarii$, nearly the same blue-shifts, $295\ \mathrm{cm}^{-1}$ and $280\ \mathrm{cm}^{-1}$, respectively, with respect to the electrochromic shift values in Table 5, are obtained. In contrast, the site energy of BChl 2, which is bound by a water bridge, shifts differently in the two bacteria. A blue-shift of $170\ \mathrm{cm}^{-1}$ results for $C.\ tepidum$, for $P.\ aestuarii$ the shift is just $100\ \mathrm{cm}^{-1}$. In other words, the energy E_0 in Eq. 55 is now assumed to depend on the ligand. The E_0^{His} for His is equal to the E_0 in Table 5, for Leu it is $E_0^{\mathrm{His}} + 295\ \mathrm{cm}^{-1}$ and $E_0^{\mathrm{His}} + 280\ \mathrm{cm}^{-1}$ in $C.\ tepidum$ and $P.\ aestuarii$, respectively, and for water it is $E_0^{\mathrm{His}} + 170\ \mathrm{cm}^{-1}$ in $C.\ tepidum$ and $E_0^{\mathrm{His}} + 100\ \mathrm{cm}^{-1}$ in $P.\ aestuarii$. A correlation plot of the electrochromic shift values (with and without partial fit) and the site energies obtained from the fit of the spectra is shown in Fig. 10. The spectra calculated are compared in Fig. 11 with the experimental data (24,25). The absorption and LD spectra fit very well, whereas for CD a much better agreement can be obtained if the direction of the Q_y-transition dipole moment is rotated by $7°$ toward the 13^1-keto-group (IUPAC-numbering) with respect to the $N_{\mathrm{I}} \rightarrow N_{\mathrm{III}}$ ($N_{\mathrm{B}} \rightarrow N_{\mathrm{D}}$) axis of the BChls.

TEMPORAL AND SPATIAL RELAXATION OF EXCITONS

In the following, the temporal and spatial relaxation of excitons is calculated in the monomeric subunit of the FMO complex of $C.\ tepidum$. The exciton dynamics in $P.\ aestuarii$ is very similar, and therefore not shown.

Delocalization of excitons

The delocalization of excitons is investigated by the disorder-averaged exciton-states pigment distribution function $d_m(\omega)$ that describes the contribution of a given pigment m to the different exciton states (42):

$$d_m(\omega) = \left\langle \sum_M |c_m^{(M)}|^2 \delta(\omega - \omega_M) \right\rangle_{\mathrm{dis}}. \qquad (56)$$
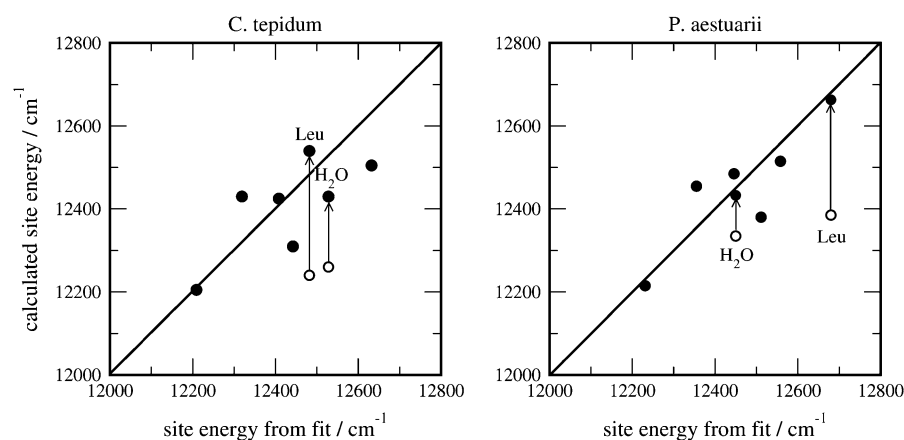
FIGURE 10 Correlation between site energies obtained from electrochromic shift calculations and fit of optical spectra, for $C.\ tepidum$ (*left*) and $P.\ aestuarii$ (*right*). The arrows indicate the shift of the electrochromic site energies of the two BChls which are not ligated by His, obtained from a partial fit as explained in the text.
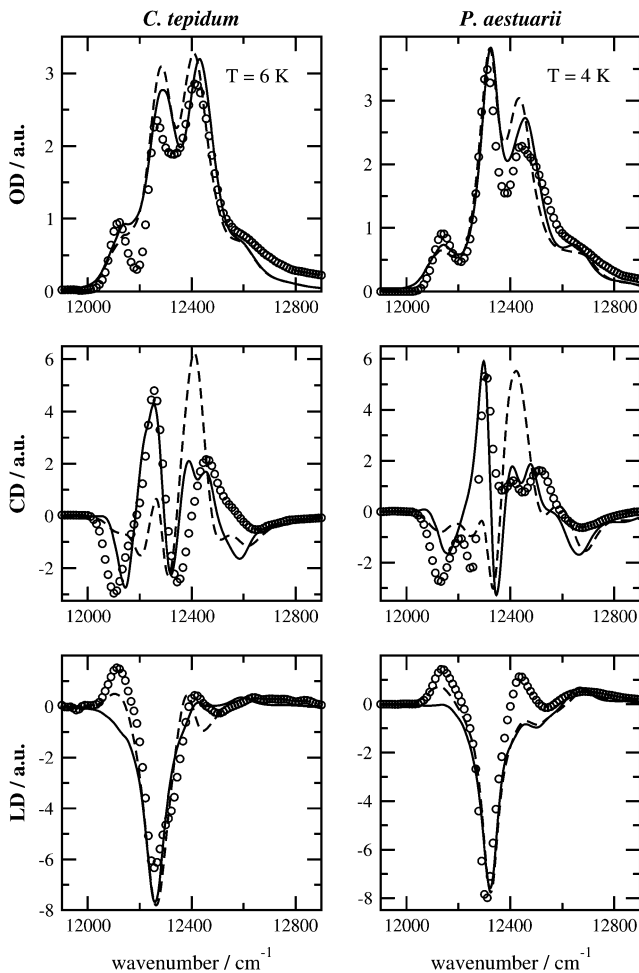
FIGURE 11 Spectra calculated for site energies from electrochromic shifts in Table 5 and partial fit of site energies of BChl 2 and 5 as explained in the text. The site energy for BChl 2 is 12,435 cm^{-1} in both complexes and that of BChl 5 amounts to 12,540 cm^{-1} for *C. tepidum* and 12,665 cm^{-1} for *P. aestuarii*. The calculations were performed for the trimer structure assuming two different angles for the tilt of the Q_y transition dipole moment of the BChls toward their 13^1-keto-group: 0° (*dashed line*) and 7° (*solid line*). Experimental data (24,25) are shown as circles and are the same as in Fig. 9.

In Fig. 12 the function $d_m(\omega)$ for the seven pigments of the FMO-monomer of *C. tepidum* is compared with the density of exciton states:

$$d_M(\omega) = \langle \delta(\omega - \omega_M) \rangle_{\text{dis}}. \qquad (57)$$

In the calculations, the site energies obtained from the genetic fit in Table 4 were used. It is seen that the excited states of the pigments contribute to more than one exciton state. BChls 1 and 2 form an excitonic hetero dimer and dominate exciton levels 3 and 6. BChls 3 and 4 dominate the two lowest exciton levels 1 and 2, and BChl 4 has additional contributions in exciton levels 4 and 5. The excited states of the remaining pigments 5–7 are distributed over 2–4 different exciton states predominantly in the blue side of the spectrum.
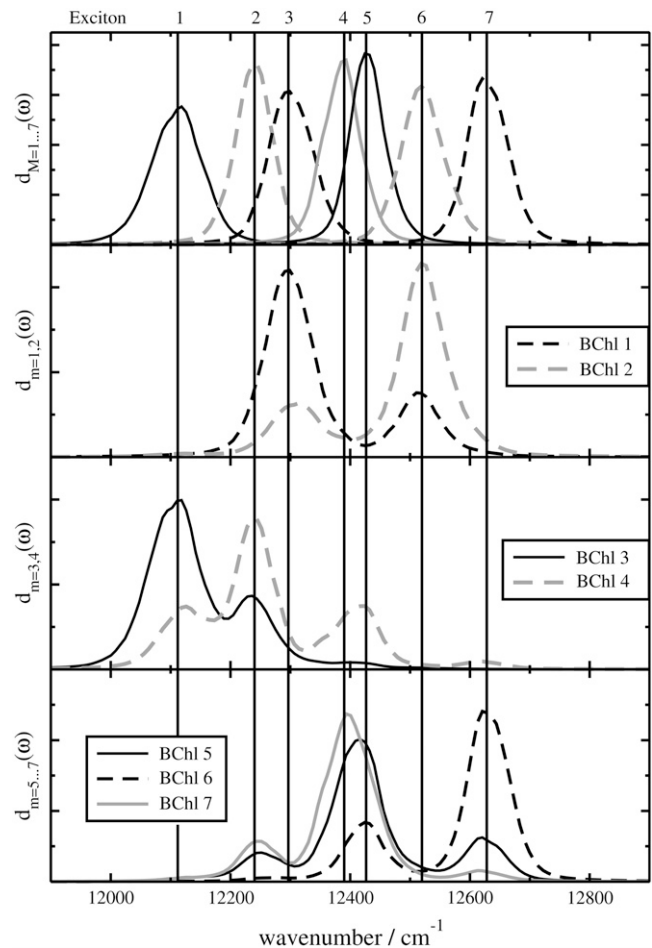

FIGURE 12 (*a*) The disorder-averaged density of exciton states $d_M(\omega)$ defined in Eq. 57. (*b,c,d*) The exciton-states pigment distribution functions $d_m(\omega)$ in Eq. 56.

Spectral density and exciton relaxation

The spectral density $S_0 J_0(\omega)$ that is used in the calculations of exciton relaxation is compared in Fig. 2 (*top*) to the vibrational sideband measured by Wendling et al. (37) on the FMO complex of *C. tepidum*. The $J_0(\omega)$ that was originally extracted from fluorescence line narrowing spectra of B777-complexes (26) is very similar to the experimental sideband measured for *C. tepidum*, the largest deviations being observed at 180 cm^{-1}. Based on this comparison a high frequency vibrational mode with a wavenumber of 180 cm^{-1} was included in the calculation of optical spectra in addition to the low-frequency part $S_0 J_0(\omega)$, as noted before.

Fig. 2 (*bottom*) contains the function $\tilde{C}^{(\text{Re})}(\omega)$ that is obtained from the spectral density $S_0 J_0(\omega)$ at the top of this figure by Eq. 21. Whereas the $S_0 J_0(\omega)$ peaks at ~20 cm^{-1} the quadratic ω dependence of $\tilde{C}^{(\text{Re})}(\omega)$ shifts the maximum to larger energies at ~200 cm^{-1}. The vertical bars at the bottom of this figure contain the function γ_{MN} in Eq. 17 at the average energetic position of the exciton transition energies
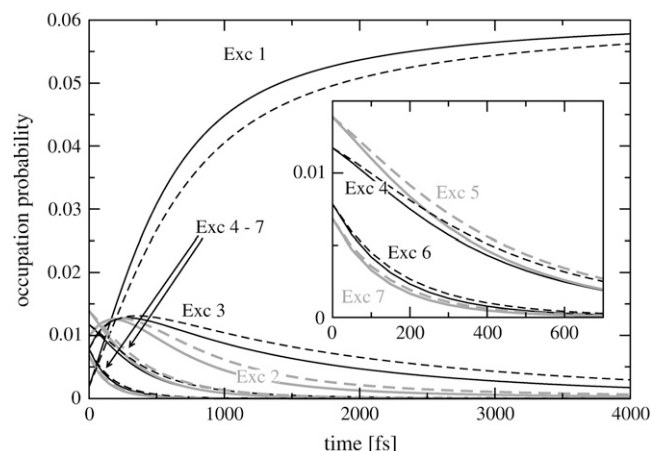
FIGURE 13 Disorder-averaged population dynamics of exciton states, after optical excitation with a 50-fs pulse centered energetically at 12,626 cm^{-1}. The solid lines were obtained using Redfield theory rate constants (Eq. 20) and the dashed lines show the modified-Redfield theory (Eq. 40) results. The inset shows an enlarged view on the occupation probabililies of exciton slaks 4–7.
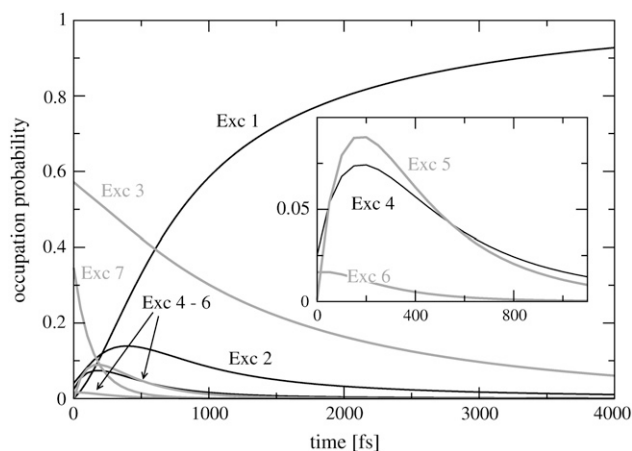

FIGURE 14 Disorder-averaged population dynamics of exciton states calculated in Redfield theory, where the initial population was created assuming that the excitation energy arrives from above the trimer in Fig. 1 as explained in detail in the text. The inset contains on enlarged view on the occupation probabilities of exciton states 4–6.

$\hbar\omega_{MN}$. The $\tilde{C}^{(\mathrm{Re})}(\omega)$ covers the whole range of transition energies between the different exciton states.

Exciton relaxation after excitation by a short pulse

The population of exciton states after initial excitation by a 50 fs (FWHM) pulse at the blue edge (12,626 cm^{-1}) of the spectrum was calculated and is shown in Fig. 13. For comparison, Redfield (*solid lines*) as well as modified Redfield (*dashed lines*) rate constants were used in the calculation of exciton relaxation. The two types of rate constants give very similar results, with the modified Redfield theory predicting slightly slower exciton relaxation. The pulse, which is spectrally broad, populates exciton levels 2–7. The high energy exciton state populations decay on a subpicosecond timescale and those of low energy on a picosecond timescale. After 4 ps the lowest state and to a very minor extent the third exciton state carry the whole excitation.

Exciton relaxation perpendicular to the trimer plane

It is finally investigated how the transfer of excitation energy occurs along the normal of the trimer plane. For this purpose as an initial condition, the exciton states with the largest contribution of pigments 1 and 6 located on the upper part of the trimer in Fig. 1 were populated, weighted by the transition dipole moment square of those exciton states. The evolution of exciton state populations $P_M(t)$ for this initial condition is shown in Fig. 14. At time zero mainly exciton states 3 and 7 are populated. The subsequent relaxation times of the two populations differ by an order of magnitude. The exciton initially on exciton state 7 relaxes within 200 fs and the one on state 3 in 2 ps. The corresponding local occupation probabil-

ities of the pigments, $P_m(t) = \sum_M |c_m^{(M)}|^2\, P_M(t)$, are shown in Fig. 1 (*bottom*), for three different times. At time zero, BChls 1, 2, 5, and 6 in the upper half of the trimer carry the excitation. After 200 fs, all the pigments are excited. At 1 ps, the excitation is localized on pigments 1–4, and after ~5 ps, the equilibrated excited state of the complex is reached where only pigments 3 and 4 at the bottom of the trimer are in the excited state.

DISCUSSION

For the first time, a convincing correlation between two independent calculation methods of pigment transition energies in proteins, the so-called site energies, is obtained. The site energies of FMO complexes from two different bacteria, *P. aestuarii* and *C. tepidum*, were obtained from a fit of optical spectra and, independently, by a calculation of electrochromic shifts due to charged amino acids. The three main results of those calculations are 1), pigment number three has the lowest site energy; 2), for pigment number five, the strongest deviation occurs between the two species; and 3), for the five BChls bound to His, BChl 6 has the largest site energy. From the two possible orientations of the FMO trimer relative to the membrane, that were identified by LD measurements on isolated FMO trimers and membrane fragments (62), only the one with BChl 3 at the bottom and BChl 6 at the top allows for an efficient transfer of excitation energy to the reaction center.

From the earlier fits (19–25), those by Vulto et al. (24) and Wendling et al. (25) predicted the correct site energies. The main difference between the present and those two earlier fits (24,25) is the use of a more advanced theory for optical spectra that results in a better agreement with experimental data, and the explanation of the low effective dipole strength used in the calculation of the excitonic couplings. The effective dipole strength $f\mu_{\mathrm{vac}}^2 = 30\ \mathrm{D}^2$ obtained here justifies the earlier use of similar low values $f\mu_{\mathrm{vac}}^2 = 29\ \mathrm{D}^2$ (24) and

$f\mu_{vac}^2 = 31\ D^2$ (25), which have been treated essentially as fit parameters. The present explanation of the effective dipole strength is based on electrostatic calculations of the Coulomb-coupling between transition charges of BChl in the dielectric environment of the protein, assuming an optical dielectric constant $\varepsilon = 2$ for the latter and a vacuum dipole strength of $\mu_{vac}^2 = 37.1\ D^2$, as determined recently by Knox and Spring (44) for the present empty cavity model. The explanation of the low effective dipole strength is important since, it seems, the use of a higher dipole strengths (51–55 D^2) prevented the other fits (19–23) from finding the right site energies.

However, for the present low effective dipole strength also, it is not guaranteed that there exists a unique fit and that there is no other set of site energies to explain the spectra. In this study we tried to minimize this possibility by a check of the genetic algorithm using calculated spectra as a test set for the algorithm. However, a real proof of the global minimum requires an independent determination of the site energies. Such a determination was achieved here by the calculation of electrochromic shifts in site energies due to charged amino acids. Although, as the correlation plot in Fig. 10 shows, there are deviations between the fitted and directly determined site energies, there is a clear correlation. In particular, the large difference in site energies between BChl 3 and BChl 6 in the genetic fit is well reproduced by the electrochromic shifts, allowing us to decide about the orientation of the FMO trimer relative to the membrane containing the reaction center. The red-shift of BChl 3 and the blue-shift of BChl 6 are caused by charged amino acids that are conserved in the two bacteria, as in, for example, the positively charged hydrogen-bond donor Arg-95 of BChl 6.

The effective dielectric constants ε_{eff} of 3.8 and 4.3 inferred from the electrochromic shift calculations for *C. tepidum* and *P. aestuarii*, respectively, are in between earlier values estimated for the two branches of bacterial reaction center (58) and agree also with values for the dielectric constant of proteins obtained independently: From molecular dynamics calculations (63,64) and normal mode calculations (65) using Kirkwood-Fröhlich dielectric theory, a dielectric constant in the range of 2–6 has been calculated for the interior of proteins. A value of $\varepsilon_{eff} = 4$ is routinely used in calculations of redox potentials of cofactors in proteins (66–69).

The major deviations between the electrostatic calculations and the fitted values of site energies are obtained for the two BChls which are not ligated by His. To take into account the effect of the ligand a partial fit was performed, where the two site energies of the pigments with non-His ligand were optimized. In agreement with mutation studies, which suggest that His ligands lead to low transition energies (3), a blue-shift of the site energy of the two BChls which are not ligated by His is obtained from the partial fit. A reason for the low transition energies of the BChls with a His ligand might be the large polarizability of the conjugated π-electrons of His that results in a large dispersive interaction (70–72), which is known to yield a red-shift of the transition energy.

Taking into account the effect of the ligand, there is an approximately equal additional blue-shift of the site energies of BChl 5, which is bound by Leu, for both *C. tepidum* and *P. aestuarii*. In contrast, the site energy of BChl 2, which is bound by a water bridge to Asn-79, shifts differently for the two species. An inspection of the water ligand of the Mg atom of BChl 2 in the structures reveals that the Mg-O distance in *C. tepidum* is 2.4 Å, whereas in *P. aestuarii* it is just 1.9 Å, a difference that might explain the different shifts of the site energies of BChl 2. A reason for the different position of the water molecule could be that one neighboring amino acid of Asn-79, which binds the water, is different in the two species. Mutation studies would be helpful to clarify this point.

The optical spectra calculated from the electrochromic and the two partially fitted site energies in Fig. 11 agree surprisingly well despite the simplicity of the model. The agreement suggests that the major contribution to the shift in site energies in the present system is from charged amino acids and the ligands. In particular, these effects explain the difference in the absorption spectra between the two bacteria, i.e., the switch in relative intensity of the two main bands. A major contributor to this switch is BChl 5, which is the only pigment for which the electrochromic shift in Table 5 has a different sign in the two species.

The largest deviation between experimental and calculated spectra occur for the CD spectra, both of *C. tepidum* and *P. aestuarii*. Those deviations might have several reasons—the neglect of site energy shifts by hydrogen bonds; by the different conformations of the pigments; and by different protonation states of the titratable groups of the protein. We are currently investigating those effects in detail. Alternatively, the deviations in the CD spectra become much smaller when a 7° rotation of the Q_y transition dipole moment of the BChls toward the 13^1-keto-group is assumed. It is interesting to note that such a rotation is discussed in the literature for bacteriochlorophyll-a (73,74) and for the related chlorophyll-a molecule (75,76). The exact value of the tilt angle is still an open question, and might depend also on the protein environment. From experiments on BChla embedded in a liquid crystal matrix, evidence was reported for a partial *x*-polarization of the Q_y transition (73), which depends on the type of matrix environment. In Georgakopoulou et al. (74), an angle of 7° has been inferred for the B850$_\alpha$ BChls of the LH2 light-harvesting complex on the basis of modeling CD data. For chlorophyll-a, from an analysis of time-resolved fluorescence anisotropy measurements on the peridinin-chlorophyll-a-protein, an angle of (4.5 ± 2.5)° was estimated (76). An angle of 20° was reported (75), based on linear dichroism experiments on chlorophyll-a oriented in a lamellar phase of glycerylmonooctanoate/H_2O.

By the tuning of site energies, the proteins can trigger the spatial and temporal way of excitons through the FMO-complex, on their way from the outer antenna, the chlorosomes, to the reaction center. Since this spatial transfer is connected with an energetic relaxation, on the basis of the

site energies determined here, we conclude that the linker pigments between the FMO complex and the reaction center are BChls 3 and 4, which form the lowest exciton state (Fig. 12) and are situated at the bottom of the trimer shown in Fig. 1. The actual calculation of exciton relaxation, either initiated by assuming an excitation by an ultrashort optical pulse or by assuming that the excitation arrives from above the trimer, where the chlorosomes are situated in vivo, reveals the occurrence of a fast subpicosecond as well as a relatively slow picosecond transfer branch of excitons between the upper part of the trimer and the bottom containing BChls 3 and 4. The fast branch involves BChls 5, 6, and 7, and the slow branch BChls 1 and 2. It is not clear whether there is a physiological significance of the difference of one order of magnitude in relaxation times between the two branches. Those different relaxation times were found also in transient absorption measurements (30,32), as discussed in the Introduction. A difference of the present calculations with respect to the earlier Redfield calculations (30) is the use of the correct $\tilde{C}^{(\mathrm{Re})}(\omega) \propto \omega^2 J(\omega)$ instead of the $\tilde{C}^{(\mathrm{Re})}(\omega) \propto J(\omega)$ that incorrectly favors relaxation between exciton states with small energy differences. In addition, the present study contains an estimation of the maximum rate constants (obtained for uncorrelated fluctuation of site energies) of exciton relaxation without using a free parameter to adjust the relaxation times (30). A difference between the present calculation of exciton relaxation with the modified Redfield/Förster theory study (32) is the use of a spectral density that was extracted from experiments and the comparison of the modified Redfield theory with the much simpler Redfield theory. The spectral density that was originally extracted from calculations of fluorescence line narrowing spectra of B777-complexes is very similar in shape to the fluorescence line narrowing spectrum measured on the FMO-complex of *C. tepidum* (Fig. 2). This similarity, which is also found with respect to spectral densities extracted for other complexes (77,78), suggests that the local modulation of pigment transition energies by the protein environment is a global quantity that does not so much differ for the specific environments of the pigments. The comparison of the relaxation dynamics obtained in modified-Redfield theory with that in Redfield theory in Fig. 13 shows that there are only minor differences. The slightly slower modified Redfield rates might be due to the barriers created between the excitonic PES due to their mutual shifts, which are neglected in Redfield theory. On the other hand, the delocalization of excited states leads to rather large off-diagonal parts of the exciton vibrational coupling, and so there are also corrections to the modified Redfield rates due to the fact that the nuclei do not relax in the excitonic PES determined solely by the diagonal part of the exciton vibrational coupling.

An advantage of Redfield theory is the simple form of the rate constant that allows us to analyze the different relaxation channels, present in the FMO complex. We focus therefore on the Redfield rate constant in Eq. 20 in the following. The latter is given as a product of the function γ_{MN} in Eq. 17 and

$\tilde{C}^{(\mathrm{Re})}(\omega_{MK})$ in Eq. 21. The former contain the exciton coefficients and the correlation radius of protein vibrations that describe, in an effective way, how the fluctuation of site energies of different pigments are correlated. In the limit $R_c \rightarrow \infty$ we have $\gamma_{MN} = \delta_{MN}$, i.e., there is no relaxation of excitons, whereas the fastest relaxation occurs for uncorrelated fluctuations of site energies. In this case $\gamma_{MN} = \sum_m |c_m^{(M)}|^2 |c_n^{(M)}|^2$, i.e., relaxation occurs between such exciton states which have contributions from the same pigments. From a comparison with relaxation data measured in transient absorption experiments (27–30) it can be concluded that the site energies of the pigments in the FMO complex fluctuate rather uncorrelatedly, i.e., $R_c < 10$ Å. Important insights into the relaxation channels are obtained by investigating the disorder-averaged exciton states pigment distribution functions $d_m(\omega)$, shown for *C. tepidum* in Fig. 12. As seen there, BChl 1 and BChl 2 form an excitonic dimer, and there are no major contributions from those two pigments in other exciton states, explaining why the γ_{31} and γ_{32} and therefore the exciton relaxation rates from exciton state 3 to the lower states are so small. In contrast, the remaining pigments via their exciton states distributions efficiently connect the remaining exciton states and lead to the fast subpicosecond relaxation times. The disorder-averaged factors γ_{MN} are shown as bars in Fig. 2 (*bottom*) together with the function $\tilde{C}^{(\mathrm{Re})}(\omega)$, which describes how well the protein vibrations can dissipate the excess energy of excitons during relaxation. The respective transition energies that occur during relaxation, depicted by the energetic position of the γ_{MN} bars, fit very well into the energetic range of the function $\tilde{C}^{(\mathrm{Re})}(\omega)$, which at low temperature is proportional to $\omega^2 J(\omega)$ with the $J(\omega)$ from Fig. 2 (*top*). It is seen thereby that the spectral density of the pigment-protein coupling is well optimized to dissipate the excess energy of excitons during relaxation.

The present method of obtaining site energies and excitonic couplings from electrostatics calculations provides an additional basis for the elucidation of structure function relationships in pigment-protein complexes and a testing ground for the development of dynamical theories. The latter will allow for a more complete comprehension of the rich information contained in the newly measured two-dimensional photon echo spectra (31,32). The present calculations of excitonic couplings show that it is very unlikely that the second strongest excitonic coupling occurring between BChl 5 and 6 in the FMO complex is reduced by almost 60%, with respect to the coupling obtained in point dipole approximation, a reduction that was inferred from the calculation of the photon-echo spectra (31,32). Neither deviations from the point dipole approximation nor the influence of the dielectric protein environment support this reduction. Cho et al. (31,32) pointed out that another approximation in the calculations of the photon-echo spectra, that could be crucial, was the neglect of electronic coherence transfer terms in the nonlinear polarization. It is interesting to note that although those terms were found to be small in the

calculations of linear absorption spectra of the LH2-light harvesting complex (79), in the calculation of nonlinear fluorescence anisotropy decay spectra on the same complex they were reported to be more important (80). Another correction that could improve the agreement between the calculated and measured photon-echo spectra concerns the detuning of two exciton state energies (81), for example, by intramolecular excited state absorption of the BChls (23).

CONCLUSIONS

Based on two independent methods, using a fit of optical spectra with a genetic algorithm, and by direct electrochromic shift calculations, the site energies of the seven BChls in the FMO monomeric subunits of the FMO-complexes of *C. tepidum* and *P. aestuarii* were determined and used to calculate the spatial and temporal relaxation of excitons. From those calculations, it can be concluded that:

1. The most important contributions to the shift in site energies are due to charged amino acids and the ligands.
2. The charged amino acids are responsible for the low site energy of BChl 3, the large site energy of BChl 6, and the large difference in site energy of BChl 5 between *C. tepidum* and *P. aestuarii*.
3. Histidine ligands lead to lower site energies than leucine or water.
4. To allow for efficient excitation energy transfer to the reaction center, the relative orientation of the FMO trimer, with respect to the reaction center, is such that BChls 3 and 4 are at the interface between the two complexes.
5. Exciton relaxation through the FMO complex between the chlorosomes and the reaction center in green sulfur bacteria occurs along a fast subpicosecond and a slow picosecond branch.

The present simple electrostatic method of calculating site energies can be readily applied to larger complexes for which an unambiguous fit of site energies from optical spectra is not possible because of the large number of pigments, and hence the large number of parameters. The advantage of an electrostatic method, compared to a solely quantum chemical method (2,9), is that the whole protein, and not just a small environment of the pigments, can be included in the calculations. At the moment, the method is developed further by performing an average over the different protonation states of the titratable groups, using a more sophisticated electrostatic description in atomic detail that is capable also of including the effect of hydrogen bonds, the influence of the charge density of the neutral amino-acid residues, and the influence of the water/glycerol dielectric environment.

SUPPLEMENTARY MATERIAL

An online supplement to this article can be found by visiting BJ Online at http://www.biophysj.org.

REFERENCES

1. Eccles, J., and B. Honig. 1983. Charged amino acids as spectroscopic determinants for chlorophyll in vivo. *Proc. Natl. Acad. Sci. USA.* 80:4959–4962.

2. Damjanovic, A., H. M. Vaswani, P. Fromme, and G. R. Fleming. 2002. Chlorophyll excitations in Photosystem I of *Synechococcus elongatus.* *J. Phys. Chem. B.* 106:10251–10262.

3. Diner, B. A., E. Schlodder, P. J. Nixon, W. J. Coleman, F. Rappaport, J. Lavergne, W. F. J. Vermaas, and D. A. Chisholm. 2001. Site-directed mutations at D1–HIS198 and D2–HIS197 of Photosystem II in *Synechocystis* PCC 6803: sites of primary charge separation and cation and triplet stabilization. *Biochemistry.* 40:9265–9281.

4. Spangler, D., G. M. Maggiora, L. L. Shipman, and R. E. Christoffersen. 1977. Stereoelectronic properties of photosynthetic and related systems. 2. Ab initio quantum mechanical ground state characterization of magnesium porphine, magnesium chlorin, and ethyl chlorophyllide-a. *J. Am. Chem. Soc.* 99:7478–7489.

5. Sturgis, J. N., and B. Robert. 1996. The role of chromophore coupling in tuning the spectral properties of peripheral light-harvesting protein of purple bacteria. *Photosynth. Res.* 50:5–10.

6. Sturgis, J. N., and B. Robert. 1997. Pigment binding-site and electronic properties in light-harvesting proteins of purple bacteria. *J. Phys. Chem. B.* 101:7227–7231.

7. Witt, H., E. Schlodder, C. Teutloff, J. Niklas, E. Bordignon, D. Carbonera, S. Kohler, A. Labahn, and W. Lubitz. 2002. Hydrogen bonding to P700: site-directed mutagenesis of threonine A739 of Photosystem I in *Chlamydomonas reinhardtii. Biochemistry.* 41:8557–8569.

8. Warshel, A., and W. W. Parson. 1987. Spectroscopic properties of photosynthetic reaction centers. I. Theory. *J. Am. Chem. Soc.* 109:6143–6152.

9. Gudowska-Nowak, E., M. D. Newton, and J. Fajer. 1990. Conformational and environmental effects on bacteriochlorophyll optical spectra: correlations of calculated spectra with structural results. *J. Phys. Chem.* 94:5795–5801.

10. Pearlstein, R., and R. P. Hemenger. 1978. Bacteriochlorophyll electronic-transition moment directions in bacteriochlorophyll a-protein. *Proc. Natl. Acad. Sci. USA.* 75:4920–4924.

11. Fenna, R. E., and B. W. Matthews. 1975. Chlorophyll arrangement in a bacteriochlorophyll protein from *Chlorobium limicola. Nature.* 258:573–577.

12. Matthews, B. W., R. E. Fenna, M. C. Bolognesi, M. F. Schmid, and J. M. Olson. 1979. Structure of a bacteriochlorophyll-a protein from the green photosynthetic bacterium *Prosthecochloris aestuarii. J. Mol. Biol.* 131:259–285.

13. Tronrud, D. E., M. F. Schmid, and B. W. Matthews. 1986. Structure and x-ray amino acid sequence of a bacteriochlorophyll-a protein from *Prosthecochloris aestuarii* refined at 1.9 Å resolution. *J. Mol. Biol.* 188:443–454.

14. Li, Y. F., W. Zhou, R. E. Blankenship, and J. P. Allen. 1997. Crystal structure of the bacteriochlorophyll-a protein from *Chlorobium tepidum. J. Mol. Biol.* 271:456–471.

15. Camara-Artigas, A., R. Blankenship, and J. P. Allen. 2002. The structure of the FMO protein from *Chlorobium tepidum* at 2.2 Å resolution. *Photosynth. Res.* 75:49–55.

16. Olson, J. M. 2004. The FMO protein. *Photosynth. Res.* 80:181–187.

17. Rémigy, H. W., H. Stahlberg, D. Fotiadis, B. Wolpensinger, A. Engel, G. Hauska, and G. Tsiotis. 1999. The reaction centre complex from green sulphur bacterium *C. tepidum*: a structural analysis by scanning transmission electron microscopy. *J. Mol. Biol.* 290:851–858.

18. Rémigy, H. W., G. Hauska, S. A. Müller, and G. Tsiotis. 2002. The reaction centre from green sulphur bacteria: progress towards structural elucidation. *Photosynth. Res.* 71:91–98.

19. Pearlstein, R. M. 1992. Theory of the optical spectra of the bacteriochlorophyll-a antenna protein trimer from *Prosthecochloris aestuarii*. *Photosynth. Res.* 31:213–226.

20. Lu, X., and R. M. Pearlstein. 1993. Simulations of *Prosthecochloris* bacteriochlorophyll-a protein optical spectra improved by parametric computer search. *Photochem. Photobiol.* 57:86–91.

21. Gülen, D. 1996. Interpretation of the excited-state structure of the Fenna-Matthews-Olson protein of the photosynthetic pigment-protein complex of *Prosthecochloris aestuarii* based on simultaneous simulation of the 4 K absorption, linear dichroism, and singlet-triplet absorption difference spectra: a possible excitonic explanation? *J. Phys. Chem.* 100:17683–17689.

22. Louwe, R. J. W., J. Vrieze, A. J. Hoff, and T. J. Aartsma. 1997. Towards an integral interpretation of the optical steady state spectra of the FMO-complex of *Prosthecochloris aestuarii*. 2. Exciton simulations. *J. Phys. Chem. B*. 101:11280–11287.

23. Renger, T., and V. May. 1998. Ultrafast exciton motion in photosynthetic antenna systems: the FMO-complex. *J. Phys. Chem. A*. 102:4381–4391.

24. Vulto, S. I. E., M. A. de Baat, R. J. W. Louwe, H. P. Permentier, T. Neef, M. Miller, H. van Amerongen, and T. J. Aartsma. 1998. Exciton simulations of optical spectra of the FMO complex from the green sulfur bacterium *Chlorobium tepidum* at 6 K. *J. Phys. Chem. B*. 102:9577–9582.

25. Wendling, M., M. A. Przyjalgowski, D. Gülen, S. I. E. Vulto, T. J. Aartsma, R. van Grondelle, and H. van Amerongen. 2002. The quantitative relationship between structure and polarized spectroscopy in the FMO complex of *Prosthecochloris aestuarii*: refining experiments and simulations. *Photosynth. Res.* 71:99–123.

26. Renger, T., and R. A. Marcus. 2002. On the relation of protein dynamics and exciton relaxation in pigment-protein complexes: an estimation of the spectral density and a theory for the calculation of optical spectra. *J. Chem. Phys.* 116:9997–10019.

27. Vulto, S. I. E., A. M. Streltsov, and T. J. Aartsma. 1997. Excited state energy relaxation in the FMO complexes of the green bacterium *Prosthecochloris aestuarii* at low temperatures. *J. Phys. Chem. B*. 101:4845–4850.

28. Freiberg, A., S. Lin, K. Timpmann, and R. E. Blankenship. 1997. Exciton dynamics in FMO bacteriochlorophyll-protein at low temperatures. *J. Phys. Chem. B*. 101:7211–7220.

29. Vulto, S. I. E., S. Neerken, R. J. W. Louwe, M. A. de Baat, J. Amesz, and T. J. Aartsma. 1998. Excited-state structure and dynamics in FMO antenna complexes from photosynthetic green sulfur bacteria. *J. Phys. Chem. B*. 102:10630–10635.

30. Vulto, S. I. E., M. A. de Baat, S. Neerken, F. R. Nowak, H. van Amerongen, J. Amesz, and T. J. Aartsma. 1999. Excited-state dynamics in FMO antenna complexes from photosynthetic green sulfur bacteria: a kinetic model. *J. Phys. Chem. B*. 103:8153–8161.

31. Brixner, T., J. Stenger, H. M. Vaswani, M. Cho, R. Blankenship, and G. R. Fleming. 2005. Two-dimensional spectroscopy of electronic couplings in photosynthesis. *Nature*. 434:625–628.

32. Cho, M., H. M. Vaswani, T. Brixner, J. Stenger, and G. R. Fleming. 2005. Exciton analysis in two-dimensional electronic spectroscopy. *J. Phys. Chem. B*. 109:10542–10556.

33. May, V., and O. Kühn. 2000. Charge and Energy Transfer Dynamics in Molecular Systems: A Theoretical Introduction. Wiley-VCH, Berlin, Germany.

34. T. Renger and R. A. Marcus. 2002. Photophysical properties of PS-2 reaction centers and a discrepancy in exciton relaxation times. *J. Phys. Chem. B*. 106:1809–1819.

35. Renger, T., V. May, and O. Kühn. 2001. Ultrafast excitation energy transfer dynamics in photosynthetic pigment-protein complexes. *Phys. Rep.* 343:138–254.

36. Renger, T., and V. May. 2000. Simulations of frequency-domain spectra: structure-function relationships in photosynthetic pigment-protein complexes. *Phys. Rev. Lett.* 84:5228–5231.

37. Wendling, M., T. Pullerits, M. A. Przyjalgowski, S. I. E. Vulto, T. J. Aartsma, R. van Grondelle, and H. van Amerongen. 2000. Electron-

vibrational coupling in the Fenna-Matthews-Olson complex of *Prosthecochloris aestuarii* determined by temperature-dependent absorption and fluorescence line-narrowing measurements. *J. Phys. Chem. B*. 104:5825–5831.

38. Knapp, E. 1984. Lineshapes of molecular aggregates—exchange narrowing and intersite correlation. *Chem. Phys.* 85:73–82.

39. Zhang, W. M., T. Meier, V. Chernyak, and S. Mukamel. 1998. Exciton-migration and three-pulse femtosecond optical spectroscopies of photosynthetic antenna complexes. *J. Chem. Phys.* 108:7763–7774.

40. Yang, M., and G. R. Fleming. 2002. Influence of phonons on exciton transfer dynamics: comparison of the Redfield, Förster, and modified Redfield equations. *Chem. Phys.* 275:355–372.

41. Renger, T., and R. A. Marcus. 2003. Variable–range hopping electron transfer through disordered bridge states: application to DNA. *J. Chem. Phys.* 107:8404–8419.

42. Raszewski, G., W. Saenger, and T. Renger. 2005. Theory of optical spectra of Photosystem II reaction centers: location of the triplet state and the identity of the primary electron donor. *Biophys. J.* 88:986–998.

43. Knox, R. S., and H. van Amerongen. 2002. Refractive index dependence of the Förster resonance excitation transfer rate. *J. Phys. Chem. B*. 106:5289–5293.

44. Knox, R. S., and B. Q. Spring. 2003. Dipole strengths in the chlorophylls. *Photochem. Photobiol.* 77:497–501.

45. Hsu, C.-P., M. Head-Gordon, T. Head-Gordon, and G. R. Fleming. 2001. Excitation energy transfer in condensed media. *J. Chem. Phys.* 114:3065–3072.

46. Brooks, B. R., R. E. Bruccoleri, B. D. Olafson, D. J. States, S. Swaminathan, and M. Karplus. 1983. CHARMM: a program for macromolecular energy, minimization, and dynamics calculations. *J. Comput. Chem.* 4:187–217.

47. Chang, J. C. 1977. Monopole effects on electronic excitation interaction between large molecules. I. Application to energy transfer in chlorophylls. *J. Chem. Phys.* 67:3901–3909.

48. Bashford, D. 1990–1998. MEAD (Macroscopic Electrostatics with Atomic Detail). Download: anonymous FTP from ftp.scripps.edu, directory pub/bashford using an FTP program. The Scripps Research Institute, La Jolla, CA.

49. Kühn, O., T. Renger, and V. May. 1996. On the theory of ultrafast exciton transfer dynamics: the chlorophyll a/b dimer. *Chem. Phys.* 204:99–114.

50. Renger, T., O. Kühn, J. Voigt, and V. May. 1996. Theory of pump-probe-spectroscopy on the light harvesting complex of Photosystem II. *J. Phys. Chem.* 100:15654–15662.

51. Kinnebrock, W. 1994. Optimierung mit genetischen und selektiven Algorithmen. Oldenbourg, Germany. Optimization with genetic and selective algorithms.

52. Pohlheim, H. 1999. Evolutionäre Algorithmen. Springer, Berlin, Heidelberg, Germany. Evolutionary algorithms.

53. Brüggemann, B., K. Sznee, V. Novoderezhkin, R. van Grondelle, and V. May. 2004. Modeling exciton dynamics in the photosynthetic antenna PS1. *J. Phys. Chem. B*. 108:13536–13546.

54. Kjellberg, P., Z. He, and T. Pullerits. 2003. Bacteriochlorophyll in electric field. *J. Phys. Chem. B*. 107:13737–13742.

55. Mulkidjanian, A. Y., D. A. Cherepanov, M. Haumann, and W. Junge. 1996. Photosystem II of green plants: topology of core pigments and redox cofactors as inferred from electrochromic difference spectra. *Biochemistry*. 35:3093–3107.

56. Beekman, L. M. P., R. N. Frese, G. J. S. Fowler, R. Picorel, R. J. Cogdell, I. H. M. van Stokkum, C. N. Hunter, and R. van Grondelle. 1997. Characterization of the light-harvesting antennas of photosynthetic purple bacteria by Stark spectroscopy. 2. LH2 complexes: influence of the protein environment. *J. Phys. Chem. B*. 101:7293–7301.

57. Renge, I. 1993. Solvent effects on the visible absorption maxima of tetrapyrrolic pigments. *J. Phys. Chem.* 97:6582–6589.

58. Steffen, M., K. Lao, and S. Boxer. 1994. Dielectric asymmetry in the photosynthetic reaction center. *Science*. 264:810–816.

59. MacKerell, A. D., Jr., D. Bashford, M. Bellott, R. L. Dunbrack, Jr., J. D. Evanseck, M. J. Field, S. Fischer, J. Gao, H. Guo, S. Ha, D. Joseph-McCarthy, L. Kuchnir, K. Kuczera, F. T. K. Lau, C. Mattos, S. Michnick, T. Ngo, D. T. Nguyen, B. Prodhom, W. E. Reiher III, B. Roux, M. Schlenkrich, J. C. Smith, R. Stote, J. Straub, M. Watanabe, J. Wiorkiewicz-Kuczera, D. Yin, and M. Karplus. 1998. All-atom empirical potential for molecular modeling and dynamics studies of proteins. *J. Phys. Chem. B*. 102:3586–3616.

60. Lockhart, D. J., and S. G. Boxer. 1987. Magnitude and direction of the change in dipole moment associated with excitation of the primary electron donor in *Rhodopseudomonas sphaeroides* reaction centers. *Biochemistry*. 26:664–668.

61. Reference deleted in proof.

62. Melkozernov, A. N., J. M. Olson, Y. F. Li, J. P. Allen, and R. E. Blankenship. 1998. Orientation and excitonic interactions of the Fenna-Matthews-Olson bacteriochlorophyll-a protein in membranes of the green sulfur bacterium *Chlorobium tepidum*. *Photosynth. Res.* 56:315–328.

63. Simonson, T., and I. C. L. Brooks. 1996. Charge screening and the dielectric constant of proteins: insights from molecular dynamics. *J. Am. Chem. Soc.* 118:8452–8458.

64. Simonson, T. 2003. Electrostatics and dynamics of proteins. *Rep. Prog. Phys.* 66:737–787.

65. Gilson, M. K., and B. H. Honig. 1986. The dielectric constant of a folded protein. *Biopolymers*. 25:2097–2119.

66. Honig, B. H., and A. Nicholls. 1995. Classical electrostatics in biology and chemistry. *Science*. 268:1144–1149.

67. Ullmann, G. M., and E. W. Knapp. 1999. Electrostatic models for computing protonation and redox equilibria in proteins. *Eur. Biophys. J.* 28:533–550.

68. Rabenstein, B., G. M. Ullmann, and E. W. Knapp. 2000. Electron transfer between the Quinones in the photosynthetic reaction center and its coupling to conformational changes. *Biochemistry*. 39:10487–10496.

69. Ishikita, H., and E. Knapp. 2004. Variation of Ser-L223 hydrogen bonding with the QB redox state in reaction centers from *Rhodobacter sphaeroides*. *J. Am. Chem. Soc.* 126:8059–8064.

70. Heinz, H., U. W. Suter, and E. Leontidis. 2001. Simple and accurate computations of solvatochromic shifts in $\pi \rightarrow \pi*$ transitions of aromatic chromophores. *J. Am. Chem. Soc.* 123:11229–11236.

71. Bayliss, N. S. 1950. The effect of the electrostatic polarization of the solvent on electronic absorption spectra in solution. *J. Chem. Phys.* 18:292–296.

72. Longuet-Higgens, H. C., and J. A. Pople. 1957. Electronic spectral shifts of nonpolar molecules in nonpolar solvents. *J. Chem. Phys.* 27:192–194.

73. Bauman, D., and D. Wrobel. 1980. Dichroism and polarized fluorescence of chlorophyll-a, chlorophyll-c and bacteriochlorophyll-a dissolved in liquid crystals. *Biophys. Chem.* 12:83–91.

74. Georgakopoulou, S., R. N. Frese, E. Johnson, C. Koolhaas, R. J. Cogdell, R. van Grondelle, and G. van der Zwan. 2002. Absorption and CD spectroscopy and modeling of various LH2 complexes from purple bacteria. *Biophys. J.* 82:2184–2197.

75. Fragata, M., B. Norden, and T. Kurucsev. 1988. Linear dichroism (250–700 nm) of chlorophyll-a and pheophytine-a oriented in a lamellar phase of glycerylmonooctanoate/H$_2$O. *Photochem. Photobiol.* 47:133–143.

76. Kleima, F. J., E. Hofmann, B. Gobets, I. H. M. van Stokkum, R. van Grondelle, K. Diederichs, and H. van Amerongen. 2000. Förster excitation energy transfer in peridinin-chlorophyll-a-protein. *Biophys. J.* 78:344–353.

77. Pullerits, T., R. Monshouwer, F. van Mourik, and R. van Grondelle. 1995. Temperature dependence of electron-vibronic spectra of photosynthetic systems. *Chem. Phys.* 194:395–407.

78. Pieper, J., J. Voigt, G. Renger, and G. J. Small. 1999. Analysis of phonon structure in line-narrowed optical spectra. *Chem. Phys. Lett.* 310:296–302.

79. Jang, S., M. D. Newton, and R. J. Silbey. 2004. Multichromophoric Förster resonance energy transfer. *Phys. Rev. Lett.* 92:218301.

80. Kühn, O., V. Sundström, and T. Pullerits. 2002. Fluorescence depolarization dynamics in the B850 complex of purple bacteria. *Chem. Phys.* 275:15–30.

81. Kjellberg, P., and T. Pullerits. 2006. Tree-pulse photon echo of an excitonic dimer modeled via Redfield theory. *J. Chem. Phys.* 124: 024106-1–024106-9.